




Manipulation of parity and polarization through structural distortion in light-emitting halide double perovskites

Tamilselvan Appadurai¹, Ravi Kashikar², Poonam Sikarwar¹, Sudhadevi Antharjanam ³,
Birabar Ranjit Kumar Nanda ^{2,4,5}✉ & Aravind Kumar Chandiran ^{1,6}✉

Halide perovskite materials recently attracted wide attention for light-emitting applications. The intense white light emission and excited state lifetimes greater than 1 μs are the hallmarks of a good light-emitting material. Here, we provide a clear design strategy to achieve both of these aforementioned properties in a single material via the introduction of octahedral asymmetry in halide double perovskites $\text{Cs}_2\text{AgMCl}_6$ through iso-trivalent substitution at the M site. In the substituted $\text{Cs}_2\text{AgMCl}_6$, the presence of mixed M^{3+} sites distorts the $[\text{AgCl}_6]^{5-}$ octahedra, affecting the parity of the valence and conduction band edges and thereby altering the optical transitions. The distortion also creates a local polarization that leads to an effective photogenerated carrier separation. Considering perovskite series with three M^{3+} cations, namely Bi^{3+} , In^{3+} and Sb^{3+} , the mixed trivalent cationic compounds with specific ratios of In^{3+} and Bi^{3+} show white light emission with intensity nearly 150 times larger than that of the parent compounds, and are characterised by excited state lifetimes nearing 1 μs . Using single crystal X-ray diffraction, far-infrared absorption, steady-state and time-resolved photoluminescence, bias-dependent photoluminescence, P-E loop traces and density-functional theory calculations, we hence demonstrate the role of octahedral distortion in enhancing white light emission and excited state lifetimes of halide double perovskites.

¹Department of Chemical Engineering, Indian Institute of Technology Madras, Adyar, Chennai, India. ²Condensed Matter Theory and Computational Lab, Department of Physics, Indian Institute of Technology Madras, Adyar, Chennai, India. ³Sophisticated Analytical Instrument Facility, Indian Institute of Technology Madras, Adyar, Chennai, India. ⁴Centre for Atomistic Modelling and Materials Design, Indian Institute of Technology Madras, Adyar, Chennai, India. ⁵Functional Oxide Research Group, Indian Institute of Technology Madras, Adyar, Chennai, India. ⁶Centre for Photo- and Electro-Chemical Energy Sciences & Technology (C-PEC), Indian Institute of Technology Madras, Adyar, Chennai, India. ✉email: nandab@iitm.ac.in; aravindkumar@iitm.ac.in

In recent times, the family of lead-free halide double perovskites, $\text{Cs}_2\text{AgM}^{3+}\text{X}_6$ ($\text{M}^{3+} = \text{In}, \text{Bi}, \text{and Sb}$; $\text{X} = \text{halide ions}$) semiconductors have emerged as a new class of compounds with optoelectronic properties comparable to or better than that of ABX_3 halide perovskite materials. Having the advantages of superior material stability in the ambient environment, long carrier lifetime, and free of toxic lead, double-perovskite materials have shown promising applications in solar cells, X-ray detectors, photodetectors, photocatalysis, and CO_2 reduction^{1–9}. Among various double-perovskite materials, special attention has been paid to chloride-based compounds; $\text{Cs}_2\text{AgBiCl}_6$ (CABC), $\text{Cs}_2\text{AgInCl}_6$ (CAIC), and $\text{Cs}_2\text{AgSbCl}_6$ (CASC) that are crystallizing in the cubic structure. However, each of these materials has different optical properties due to direct/indirect bandgap or parity allowed/forbidden transitions that make them distinguishable^{5,10–12}. Irrespective of the nature of the bandgap, CABC and CAIC show low-intensity photoluminescence spectra with broad emission under UV irradiation, which is a unique and interesting property of these semiconductor materials^{5,13}.

In general, semiconductor materials having broad emission spectra can be effectively used in white light-emitting diodes though a broad emission is rarely observed from the single-source material. This rare family includes some semiconducting quantum dots, a few organic–inorganic 2D halide perovskite compounds, and single molecular crystals^{14–18}. In CdSe quantum dots¹⁸, broadband emission originates from the surface defects. While in 2D halide perovskites^{19–21}, the formation of the self-trapped excitons (STE) is mainly responsible for producing broadband emission due to the strong coupling of electrons or holes with the phonons present in crystal lattices^{22–25}. Generally, STE exists in materials showing soft lattice. Therefore, the photogenerated charge carriers are easily self-trapped into localized states created out of noticeable lattice distortion and thus results in emission broadening and large Stokes shift. In 2D halide perovskites, lattice distortion may occur in organic or inorganic layers via the variation in the bond length or, angle and octahedral compression that favors the formation of STE, affecting the photoluminescence properties^{17,23,26}. A 2D halide perovskite (N-MEDA) PbBr_4 (N-MEDA: N^1 -methyl-ethane-1,2-diammonium), shows the emission broadening with a large Stokes shift originating from the $[\text{PbX}_6]^{4-}$ octahedra distortion²⁷. As STE might be playing a major role in broadband emission with large Stokes shift, it is desirable to engineer lattice distortion in materials through chemical substitutions or by physical methods including high pressure^{13,28,29}.

In the case of double-perovskite materials, it has been reported that applied pressure on CABC distorts the octahedra, leading to an increase in the photoluminescence peak broadening¹³. The pressure induces contraction in the $[\text{AgCl}_6]^{5-}$ octahedra giving rise to STE. Similarly, the substitution of Na^+ in CABC resulted in the broadening of emission³⁰. In pure CAIC, the broad emission was explained by the Jahn–Teller distortion that occurs in $[\text{AgCl}_6]^{5-}$ octahedra¹². In alloying compounds, $\text{Cs}_2\text{AgSb}_{1-x}\text{Bi}_x\text{Cl}_6$ nanocrystals, it has been claimed that luminescence spectra intensity gradually increases with Bi^{3+} ³¹. In $\text{Cs}_2\text{AgIn}_x\text{Bi}_{1-x}\text{Cl}_6$ nanocrystals, the Bi substitution makes a transition in the bandgap from direct to indirect. The broad emission spectra observed in this compound are attributed to change over from parity-forbidden to allowed transitions^{32–34}. The effect of crystal structure distortion on the observed changes in photoluminescence is not explored in detail. There are several literature reports with octahedral distortion in their structures, but no clear correlation between the structural distortion and optical/optoelectronic properties is established. In this combined experimental and first-principle study, we systematically induced the distortion in MX_6 octahedra in halide double perovskites and analysed the

electronic structure to develop a correlation between the distortion and optical transitions.

Distortion can be induced in a double-perovskite material by creating inter-octahedral and/or intra-octahedral asymmetry. The former may possess a symmetric octahedron, but the angle between two octahedra deviates from 180° . This distortion is induced by a larger A-site cation and is predominantly observed in two-dimensional halide perovskites¹⁶. The intra-octahedral distortion, on the other hand, is the asymmetry created within the octahedra. In the double perovskites, $\text{Cs}_2\text{M}^{\text{A}}\text{M}^{\text{B}}\text{Cl}_6$, the octahedra formed by $\text{M}^{\text{A}}\text{Cl}_6$ and $\text{M}^{\text{B}}\text{Cl}_6$ are symmetric, and also, the angle between these two octahedra is 180° , where M^{A} is a $1+$ cation and M^{B} is a $3+$ cation. The chains connecting the metal centers are arranged in the following fashion: $-\text{Cl}-\text{M}^{\text{A}}-\text{Cl}-\text{M}^{\text{B}}-\text{Cl}-\text{M}^{\text{A}}-\text{Cl}-$. However, if a homogeneous mixture of M^{B} , say $\text{M}^{\text{B}1}$ and $\text{M}^{\text{B}2}$ is used, due to differences in the $\text{M}^{\text{B}1}-\text{Cl}$ and $\text{M}^{\text{B}2}-\text{Cl}$ bond lengths the $\text{M}^{\text{A}}\text{Cl}_6$ octahedra will be distorted and it is the strategy utilized in this work to create white light emission. The $\text{Cs}_2\text{AgM}^{\text{B}}\text{Cl}_6$ with $\text{M}^{\text{B}} = \text{Bi}^{3+}, \text{In}^{3+}$ and Sb^{3+} is selected. The strength and nature of distortion in $[\text{AgCl}_6]^{5-}$ octahedron due to the mixture of $\text{Bi}^{3+}/\text{In}^{3+}$, $\text{Bi}^{3+}/\text{Sb}^{3+}$, and $\text{In}^{3+}/\text{Sb}^{3+}$, and subsequently its effect on the optical properties is investigated^{33,35}.

Here, we carefully carried out various optical and polarization measurements to clearly correlate the effect of octahedral distortion on the (i) electronic transitions-direct/indirect and allowed/forbidden transitions and (ii) induced local polarization that affects the charge separation. To unambiguously prove the effect of distortion, we artificially created a distortion in symmetric structures by applying an electric field and investigated their optical properties. Upon the application of the electric field, the emission properties vary significantly; however, on removing the voltage bias, the material tends to revert back to its initial properties. To date, to the best of the authors' knowledge, this is the first paper on halide perovskites that reports the effect of electric bias on emission properties.

Results and discussion

Structural properties of halide double perovskites. There are at least 20 different compounds synthesized for this study, so to avoid confusion, we follow the following naming convention in the manuscript text. The end members $\text{Cs}_2\text{AgBiCl}_6$, $\text{Cs}_2\text{AgInCl}_6$, and $\text{Cs}_2\text{AgSbCl}_6$ are denoted as CABC, CAIC, and CASC, respectively. The material with mixed $3+$ sites, $\text{Cs}_2\text{AgM}_x\text{N}_y\text{Cl}_6$, will be denoted as M_xN_y , for example, $\text{Cs}_2\text{AgBi}_{0.5}\text{In}_{0.5}\text{Cl}_6$ will be denoted as $\text{Bi}_{0.5}\text{In}_{0.5}$. However, in some places, the complete compound name may be used.

Single crystals of the $\text{Cs}_2\text{AgMCl}_6$ ($\text{M} = \text{In}^{3+}, \text{Bi}^{3+}$, and Sb^{3+}) parent compounds and $3+$ mixed cationic perovskites $\text{Cs}_2\text{AgIn}_{0.5}\text{Bi}_{0.5}\text{Cl}_6$, $\text{Cs}_2\text{AgIn}_{0.5}\text{Sb}_{0.5}\text{Cl}_6$, and $\text{Cs}_2\text{AgBi}_{0.5}\text{Sb}_{0.5}\text{Cl}_6$ were grown by hydrothermal method and their structures were investigated using single-crystal X-ray diffraction. The parent compounds crystallized in $\text{Fm}\bar{3}\text{m}$, as reported previously^{12,36,37}, where the structures consist of a series of octahedra formed by alternating $[\text{AgCl}_6]^{5-}$ and $[\text{M}^{3+}\text{Cl}_6]^{3-}$. The Cs^+ ions occupy the void formed between octahedra. While the octahedra have perfect O_h symmetry, because of the difference in the $\text{Ag}-\text{Cl}$ and $\text{M}-\text{Cl}$ bond lengths, the sizes of their respective octahedra differ. In the case of CAIC, the bond distance between Ag and Cl is $2.727(3)$ Å, whereas for $\text{In}-\text{Cl}$ it is $2.514(3)$ Å. Hence, the octahedron formed by $[\text{InCl}_6]^{3-}$ is smaller than the $[\text{AgCl}_6]^{5-}$. The bond distances of $\text{Ag}-\text{Cl}$ and $\text{Bi}-\text{Cl}$ in CABC are nearly the same, $2.6962(9)$ Å and $2.6813(9)$ Å, respectively. For CASC, the $\text{Ag}-\text{Cl}$ and $\text{Sb}-\text{Cl}$ bond lengths are $2.7111(17)$ Å and $2.6290(17)$ Å, respectively. So the difference in the sizes of octahedra formed by $[\text{AgCl}_6]^{5-}$ and $[\text{M}^{3+}\text{Cl}_6]^{3-}$, is higher in CAIC followed by CASC and CABC

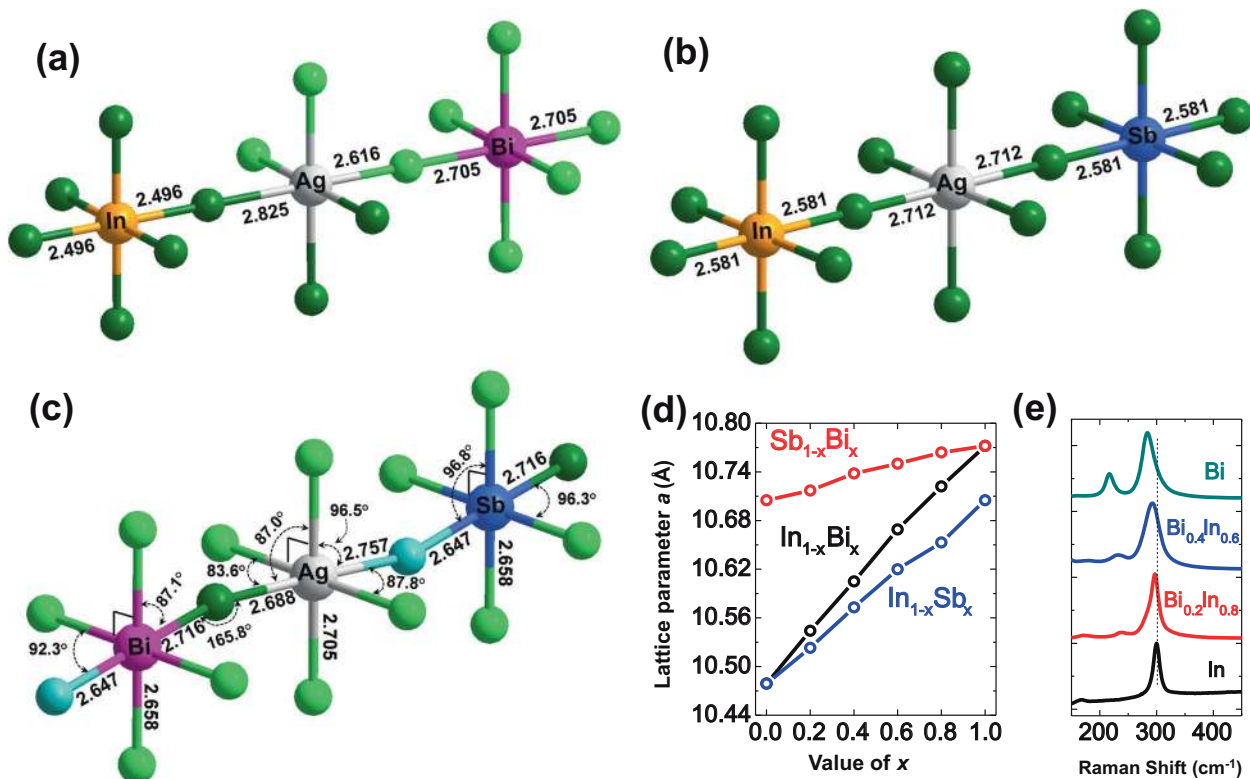


Fig. 1 Structural characterization of halide double perovskite compounds. Single crystal X-ray structures: octahedral arrangements in (a) $\text{Cs}_2\text{AgIn}_{0.5}\text{Bi}_{0.5}\text{Cl}_6$, (b) $\text{Cs}_2\text{AgIn}_{0.5}\text{Sb}_{0.5}\text{Cl}_6$, and (c) $\text{Cs}_2\text{AgSb}_{0.5}\text{Bi}_{0.5}\text{Cl}_6$ halide double perovskites compounds. (d) Calculated lattice parameters for $\text{Cs}_2\text{AgIn}_x\text{Bi}_{1-x}\text{Cl}_6$, $\text{Cs}_2\text{AgIn}_x\text{Sb}_{1-x}\text{Cl}_6$, and $\text{Cs}_2\text{AgSb}_x\text{Bi}_{1-x}\text{Cl}_6$ for various x values. (e) Raman spectra of $\text{Cs}_2\text{AgIn}_x\text{Bi}_{1-x}\text{Cl}_6$ powders for selected x values (0, 0.6, 0.8, and 1).

(Supplementary Fig. 1). Our DFT-optimized structure yields similar qualitative variations in the bond lengths, as can be observed from Supplementary Table 1. Therefore, if we make compounds with a mix of Bi^{3+} and In^{3+} , to form $\text{Cs}_2\text{AgBi}_x\text{In}_{1-x}\text{Cl}_6$, then the distortion is expected to be higher since we are mixing octahedra of different sizes at the M site.

Like the parent compounds, the mixed 3+ cationic compound $\text{Bi}_{0.5}\text{In}_{0.5}$, also crystallizes in the $\text{Fm}\bar{3}\text{m}$ -space group. However, a key difference lies in the symmetry of the $[\text{AgCl}_6]^{5-}$ octahedron that is formed between $[\text{BiCl}_6]^{3-}$ and $[\text{InCl}_6]^{3-}$ octahedra. The bond distance between In and Cl is 2.496(7) Å, whereas that of Bi and Cl is larger, 2.705(8) Å, and these bond distances reflect their corresponding lengths in their parent compounds. The $[\text{AgCl}_6]^{5-}$ octahedra are alternated between $[\text{BiCl}_6]^{3-}$ and $[\text{InCl}_6]^{3-}$, among these, three of the chloride ions in $[\text{AgCl}_6]^{5-}$ octahedron are shared with $[\text{BiCl}_6]^{3-}$ and the rest three with $[\text{InCl}_6]^{3-}$. The Cl^- shared with Bi^{3+} encounters a compression, whereas the ones shared with In^{3+} encounter an expansion due to the bigger and smaller bond lengths of Bi–Cl and In–Cl, respectively. This led to two distinct Ag–Cl bonds with bond distances of 2.825(7) Å and 2.616(8) Å, for the Cl^- shared with In^{3+} and Bi^{3+} , respectively (Fig. 1a). In the case of $\text{In}_{0.5}\text{Sb}_{0.5}$ (Fig. 1b), which also crystallized in $\text{Fm}\bar{3}\text{m}$, the In–Cl bond expanded and Sb–Cl contracted from their parent counterparts and in this mixed trivalent compound, the bond distance remained the same (2.5807(18) Å). The $[\text{AgCl}_6]^{5-}$ octahedra remained symmetric with Ag–Cl bond distance of 2.7122(18) Å. The compound formed by the mixture of Bi^{3+} and Sb^{3+} , $\text{Bi}_{0.5}\text{Sb}_{0.5}$ underwent significant distortion leading to a lowering in the symmetry to $\text{Fm}\bar{3}$. Three distinct chloride ions were found, with 4 Cl^- in-plane (represented as light-green spheres in Fig. 1c) with Bi^{3+} , Ag^+ , or Sb^{3+} resembling a square planar architecture. However, the chloride ions shared

between Bi^{3+} and Ag^+ and between Ag^+ and Sb^{3+} are unique in one of the directions (represented in dark green and sky blue in Fig. 1c) with a twist angle of 165.8° between $[\text{BiCl}_6]^{3-}/[\text{SbCl}_6]^{3-}$ and $[\text{AgCl}_6]^{5-}$ octahedra. The four Cl^- in-plane with the central metal ion (Ag/Sb/Bi) have the same bond distances, whereas the other two Cl^- have two different bond distances. Overall, the compound $\text{In}_{0.5}\text{Sb}_{0.5}$ is heavily distorted, both within and between the octahedra formed by $[\text{AgCl}_6]^{5-}$, $[\text{BiCl}_6]^{3-}$, and $[\text{SbCl}_6]^{3-}$. The CIF files of parent compounds and 3+ mixed cationic compounds are given in Supplementary Data 1 to Supplementary Data 6. The distortion in an octahedron can be quantified using the following formula:

$$\Delta d = (1/6)\sum[(d_n - \langle d \rangle)/\langle d \rangle]^2 \quad (1)$$

where $\langle d \rangle$ and d_n are the average and individual bond lengths, respectively^{24,38}. For a symmetric octahedron, the value of Δd is equal to zero representing no distortion. In the sample with the mix of In^{3+} and Bi^{3+} cations, the $[\text{AgCl}_6]^{5-}$ octahedra are asymmetric due to two distinct bond distances and the value of Δd for this octahedron is found to be 14.75×10^{-4} . Similarly, another asymmetric octahedron is found for the Bi/Sb mixed compound, where the value of distortion is found to be 0.63×10^{-4} . It has to be noted that in the latter sample, the bond angles deviate from 90° or 180°, but the formula used to calculate the distortion does not take into account this difference in the angles between atoms. So the actual distortion calculated for $\text{Bi}_{0.5}\text{Sb}_{0.5}$ sample is expected to be different. Although we expected that the alloy of Bi^{3+} or Sb^{3+} with In^{3+} is expected to distort more, due to shorter In–Cl bond length compared with Bi–Cl, Sb–Cl, or Ag–Cl, where their corresponding bond lengths remain fairly close to each other, experimentally, we find $\text{Bi}_{0.5}\text{Sb}_{0.5}$ also distorted even lowering the symmetry from $\text{Fm}\bar{3}\text{m}$ to $\text{Fm}\bar{3}$. The origin of this distortion is not

clear. The distortion factor for $[\text{AgCl}_6]^{5-}$ in $\text{In}_{0.5}\text{Bi}_{0.5}$ is at least 23 times higher than $\text{Bi}_{0.5}\text{Sb}_{0.5}$. The $\text{In}_{0.5}\text{Sb}_{0.5}$ sample on the other hand remains perfectly symmetric.

Following the analysis of single crystals, we synthesized powders using similar hydrothermal synthesis for all the optical and polarization studies. Supplementary Figure 2 to Supplementary Figure 4 show the powder XRD patterns of the $\text{Cs}_2\text{AgIn}_x\text{Bi}_{1-x}\text{Cl}_6$, $\text{Cs}_2\text{AgIn}_x\text{Sb}_{1-x}\text{Cl}_6$, and $\text{Cs}_2\text{AgBi}_x\text{Sb}_{1-x}\text{Cl}_6$ and powder compounds, with x ranging from 0 to 1. The diffraction patterns generated from the single-crystal structures match the experimental PXRD patterns of all the samples (Supplementary Fig. 5). However, it has to be noted that for the $\text{Bi}_x\text{Sb}_{1-x}$, the value of x at which the transition from $\text{Fm}\bar{3}\text{m}$ to $\text{Fm}\bar{3}$ space group is not clear. So the simulated XRD patterns of the parent compounds with $\text{Fm}\bar{3}\text{m}$ are compared with the mixed trivalent cationic compounds. A systematic shift in the peak positions for various mixed 3+ cation ratios is observed¹⁰. The lattice parameters obtained by refining the XRD plots are given in Fig. 1d and the fit data are provided in Supplementary Fig. 6 to Supplementary Fig. 8 and Supplementary Table 2 to Supplementary Table 4. For $\text{Cs}_2\text{AgIn}_x\text{Bi}_{1-x}\text{Cl}_6$, there is a notable shift in diffraction peaks to higher angles as the x is varied from 0 to 1, where the lattice parameter decreased from 10.772 Å to 10.479 Å. This shall be attributed to the lower ionic radius of In^{3+} ($r_{\text{In}} = 0.8$ Å) compared with Bi^{3+} ($r_{\text{Bi}} = 1.03$ Å)³⁹. A similar linear increase in the lattice parameters is observed for $\text{In}_x\text{Sb}_{1-x}$ and $\text{Bi}_x\text{Sb}_{1-x}$ perovskites^{33,40}. For $\text{Bi}_x\text{Sb}_{1-x}$, the expansion of lattice with the increase in the bismuth concentration is reminiscent of the higher ionic radius of Bi^{3+} , similar to the case of $\text{Bi}_x\text{In}_{1-x}$. However, in the case of $\text{In}_x\text{Sb}_{1-x}$ series, although Sb^{3+} ($r_{\text{Sb}} = 0.76$ Å) has a lower ionic radius, the increase in the concentration of Sb expands the lattice cell. Unlike $\text{In}_x\text{Bi}_{1-x}$ and $\text{Bi}_x\text{Sb}_{1-x}$, the linear increase in the lattice parameter cannot be attributed to the ionic radii alone. It may also arise from the difference in the polarizability between the two ions. In all three cases, the linear variation suggests that the uniform distribution of mixed 3+ cations satisfies Vegard's law^{41,42}.

Although PXRD provides information about the variation in the lattice parameters in powder samples, to confirm the variation in bond lengths that appeared in $[\text{AgCl}_6]^{5-}$ octahedra, like in the single crystals, we performed the Raman and FTIR (the results showed latter in the manuscript) measurements. Figure 1e shows the Raman spectra of selected $\text{Cs}_2\text{AgIn}_x\text{Bi}_{1-x}\text{Cl}_6$ powders. The Raman peaks at 217.5 and 283 cm^{-1} for CABC can be assigned to E_g and A_{1g} Raman vibrational modes. Recent studies of $\text{Cs}_2\text{AgIn}_x\text{Bi}_{1-x}\text{Cl}_6$ nanocrystals also confirm that higher strain should always be produced on Ag–Cl bonds compared with the trivalent ion bonded to chloride ions. Our observations of Raman peak intensities as well as their peak positions are in good agreement with reported literature⁴⁰. During In^{3+} ion substitution, A_{1g} symmetric vibration modes of the Ag–Cl bonds in the $[\text{AgCl}_6]^{5-}$ octahedral peaks located at 283 cm^{-1} are shifted to a higher wavenumber (300 cm^{-1}) and also weakening the peak intensity of E_g symmetric peaks. This observation indicates that the $[\text{AgCl}_6]^{5-}$ octahedron is modified due to the presence of two different trivalent ion substitutions in its neighboring octahedra. Similar differences in the Raman peak positions are observed for $\text{In}_x\text{Sb}_{1-x}$ and $\text{Bi}_x\text{Sb}_{1-x}$ mixed double perovskites and the plots are provided in Supplementary Fig. 9 and Supplementary Fig. 10. Similar to the single-crystal studies, the difference in the Raman peaks confirms the variation in the Ag–Cl bond lengths in the powder samples⁴³.

Optical absorption properties. The mixed trivalent cations influence the absorption spectra of the compounds. For $\text{Cs}_2\text{AgIn}_x\text{Bi}_{1-x}\text{Cl}_6$, the compound with $x = 1$ shows the onset of the

absorption at 370 nm with a bandgap of 3.36 eV (Supplementary Fig. 11), and the compound with $x = 0$ shows a red-shifted absorption onset at around 515 nm. All the intermediate compositions with a mixture of Bi^{3+} and In^{3+} , have their absorption onsets between these two end members. However, it has to be noted that even with 20% substitution of In^{3+} by Bi^{3+} , the onset redshifts to ~445 nm, which is nearly 75 nm red-shifted compared with its pure In^{3+} parent compound. An increase in the x value beyond 0.2 moderately redshifts the onset by another 70 nm. The In/Sb mixture shows a similar trend in the bandgap variation as in the case of In/Bi mixture. We observe that 20% substitution of Sb^{3+} in CAIC, that is $\text{Cs}_2\text{AgIn}_{0.8}\text{Sb}_{0.2}\text{Cl}_6$, reduces the bandgap drastically from 3.36 to 2.63 eV and further increases in the Sb^{3+} , shows a small decrease in the bandgap reaching the end value of 2.28 eV (Supplementary Fig. 12)^{33,40}. In both, the prior cases, the bandgap for the intermediate compositions lies between the end members. However, for $\text{Cs}_2\text{AgBi}_x\text{Sb}_{1-x}\text{Cl}_6$, where the bandgaps of the end members are 2.4 and 2.28 eV, for $x = 1$ and 0, respectively (Supplementary Fig. 13), the samples with intermediate values of x show a bandgap lower than 2.28 eV with the lowest being 1.91 eV for $x = 0.2$. The bandgap values are shown in Supplementary Table 5 to Supplementary Table 7.

To understand the optical properties of these double perovskites, density-functional theory calculation was carried out. The band structure of the pure compounds CAIC, CABC, and CASC, calculated using the experimental crystal structures, are shown in Fig. 2. DFT calculations are carried out with PBE-GGA exchange-correlation functional and mBJ potential as implemented in WIEN2k⁴⁴. The detailed computational methods are presented in the Methods section. Agreeing with the experimental observations, these compounds stabilize in the insulating phase. The calculated bandgap values are 3.3, 2.57, and 2.4 eV for CAIC, CABC, and CASC, respectively, which are very close to the respective experimental values of 3.3, 2.4, and 2.28 eV. While for CAIC, the bandgap is direct, the other two are indirect in nature.

The nature of chemical (covalent) bonding in this family of compounds is examined in detail and summarized through a schematic illustration of a molecular orbital picture (MOP) (Fig. 2b) to gain insight into the valence and conduction band spectrum. The deterministic covalent hybridizations are Ag- $\{s, e_g\}$ -Cl-p and M- $\{s, p\}$ -Cl-p (M: Bi, In, or Sb). The Cl-p-dominated bonding states are occupied. Therefore, the composition of the VBM and CBM depends on the filling of the antibonding states. Any change in it affects the parity and hence the optical transition in the system.

In the case of CAIC, dominantly, the Ag- e_g states form the valence band maximum (VBM) along the path Γ -X and the In-s state forms the conduction band minimum (CBM). In the case of CABC and CASC, the VBM is contributed both by Ag- e_g and Bi (Sb)-s orbitals. The change in the VBM composition in the latter two compounds with respect to the former is due to the fact that the free atomic energy level of In-s is approximately 5 eV higher compared with Bi (Sb)-s states. The 3+ charge state for these elements implies that In-s states are unoccupied and forming the CBM, while Bi (Sb)-s states are occupied to form the VBM and unoccupied Bi (Sb)-p states form the CBM in the respective compounds. The disparity in the dispersion between CAIC and CAB(S)C compounds comes from variation in the hybridization between Ag- e_g and In/Bi/Sb-s states as schematically illustrated in the inset Fig. 2b. In the case of CAB(S)C, the hybridized Ag- e_g (denoted as e_g'), lying higher in energy, and Bi (Sb)-s states, lying lower in energy, rehybridize to create an e_g' -dominated antibonding bands (forming the valence band edge) and s-dominated bonding bands. In the case of CAIC, the e_g' and In-s reverse their positions to create s dominated antibonding

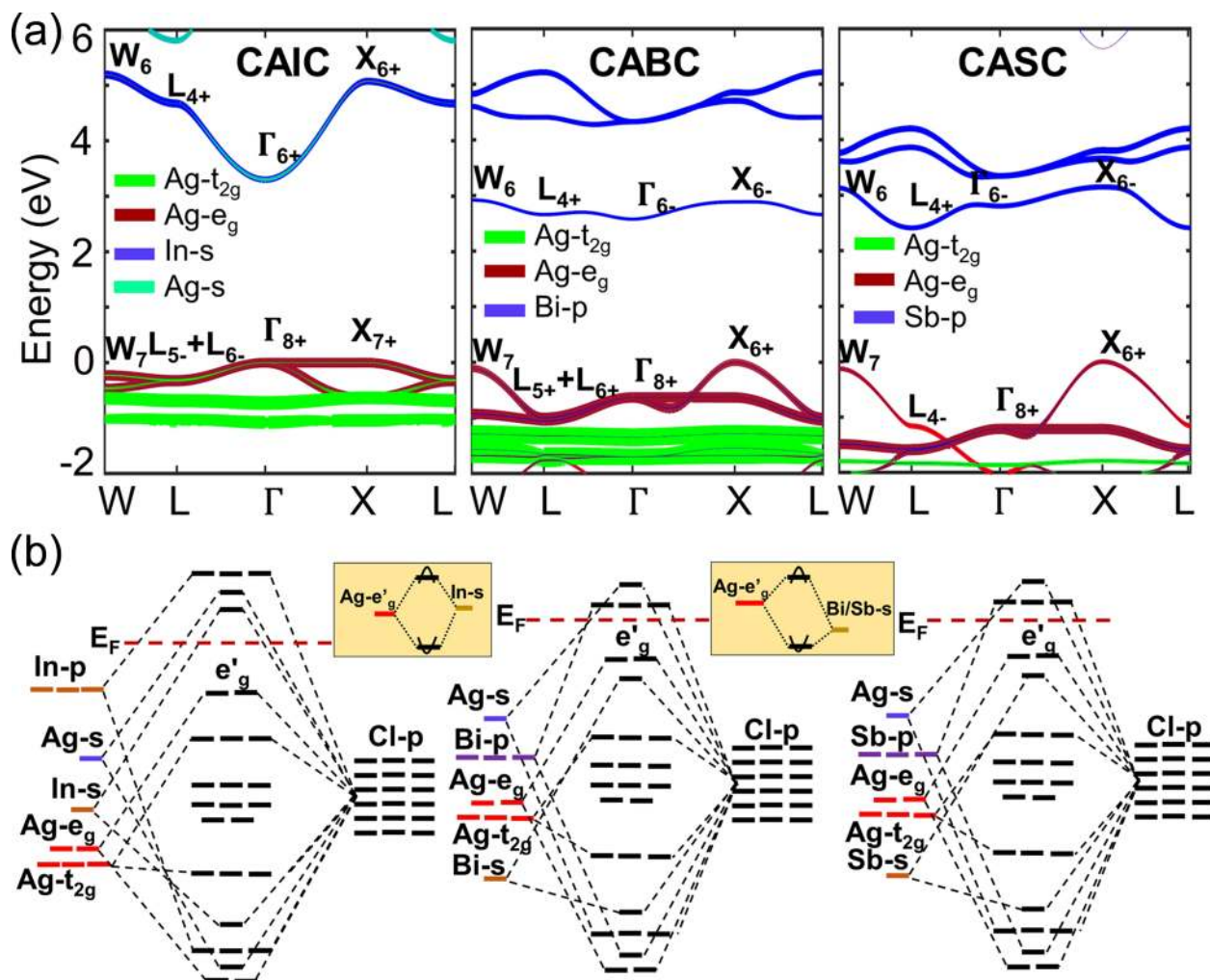


Fig. 2 Band structure of halide double perovskites. **a** Band structure of CAIC, CABC, and CASC with a display of dominant orbital characters. The parity of the valence and conduction band edges is shown in Koster notations. **b** The corresponding molecular orbital pictures as obtained by analyzing the orbital-resolved band structure and density of states (not shown here). In the inset, the nature of the hybridization among the hybridized Ag- e_g and In/Bi/Sb-s orbitals is schematically shown to distinguish the shape of the dispersion in valence and conduction band edges in these compounds.

bands and e'_g -dominated bonding bands. As a consequence, unlike the case of CASC and CABC, the valence band edge is nearly dispersionless in CAIC along k-path Γ to X direction. This reduces the dimensionality of the hole to make it heavy. The heavy hole is self-trapped to attract the electrons in the neighborhood and forms the self-trapped excitons (STE)⁴⁵.

The parity analysis of the eigenfunctions constituting the valence and conduction band edges, indicated through Koster notations in Fig. 2a, reveals that for direct bandgap compound, CAIC, the VBM, and CBM (at Γ) are of even parity. This is due to the fact that, as discussed previously, the VBM is formed by the d orbitals and CBM is formed by the s orbitals. Following Laporte's rule, the transition is allowed only between even-odd parity states and is in agreement with the previous reports⁴⁶. In the case of CABC though VBM and CBM have even-odd parities, the optical transition probability remains small due to the indirect bandgap nature. Whereas in the case of CASC the VBM and CBM are of even parity and the transitions are forbidden⁴⁷.

Steady-state photoluminescence properties. Following the investigation on absorption properties, the photoluminescence studies were carried out by exciting the materials with the photons in their respective absorption regime. The CASC, since it is an indirect bandgap semiconductor, did not show any emission. All

the mixed trivalent compounds with Sb^{3+} , that is In_xSb_{1-x} or Bi_xSb_{1-x} , quenched the emission drastically even in the presence of 20% of Sb^{3+} , although a very weak emission is observed for $In_{0.8}Sb_{0.2}$ (Supplementary Fig. 14). The band structure analysis presented later in the discussion suggests that there is a parity forbidden transition in these compositions. The presence of Sb^{3+} is detrimental to photoluminescence. The CABC is an indirect bandgap material like CASC, but it shows reasonable emission. We carried out the photoluminescence studies for $Cs_2AgIn_xBi_{1-x}Cl_6$ systematically under the given excitation conditions and compared the emission quantitatively in Fig. 3a. The end member CABC has displayed a peak centered at 575 nm with a weak but broad emission. The other end member with pure In^{3+} , also shows a broad emission with a peak centered around 600 nm.

The integrated intensity (Fig. 3b) shows that there is a one-order-of-magnitude higher emission with CAIC compared with the CABC. This is expected to arise due to the nature of the bandgap where the former is a direct and the latter is an indirect bandgap material. As the value of the x increases, that is when the In^{3+} substitution is increased in CABC; peak intensity and broadening are gradually increased up to $x = 0.7$, but at $x = 0.8$, there is a sudden jump in the emission that is more than two orders (144 times) of magnitude higher than CABC and one order (16 times) of magnitude higher than CAIC. The emission

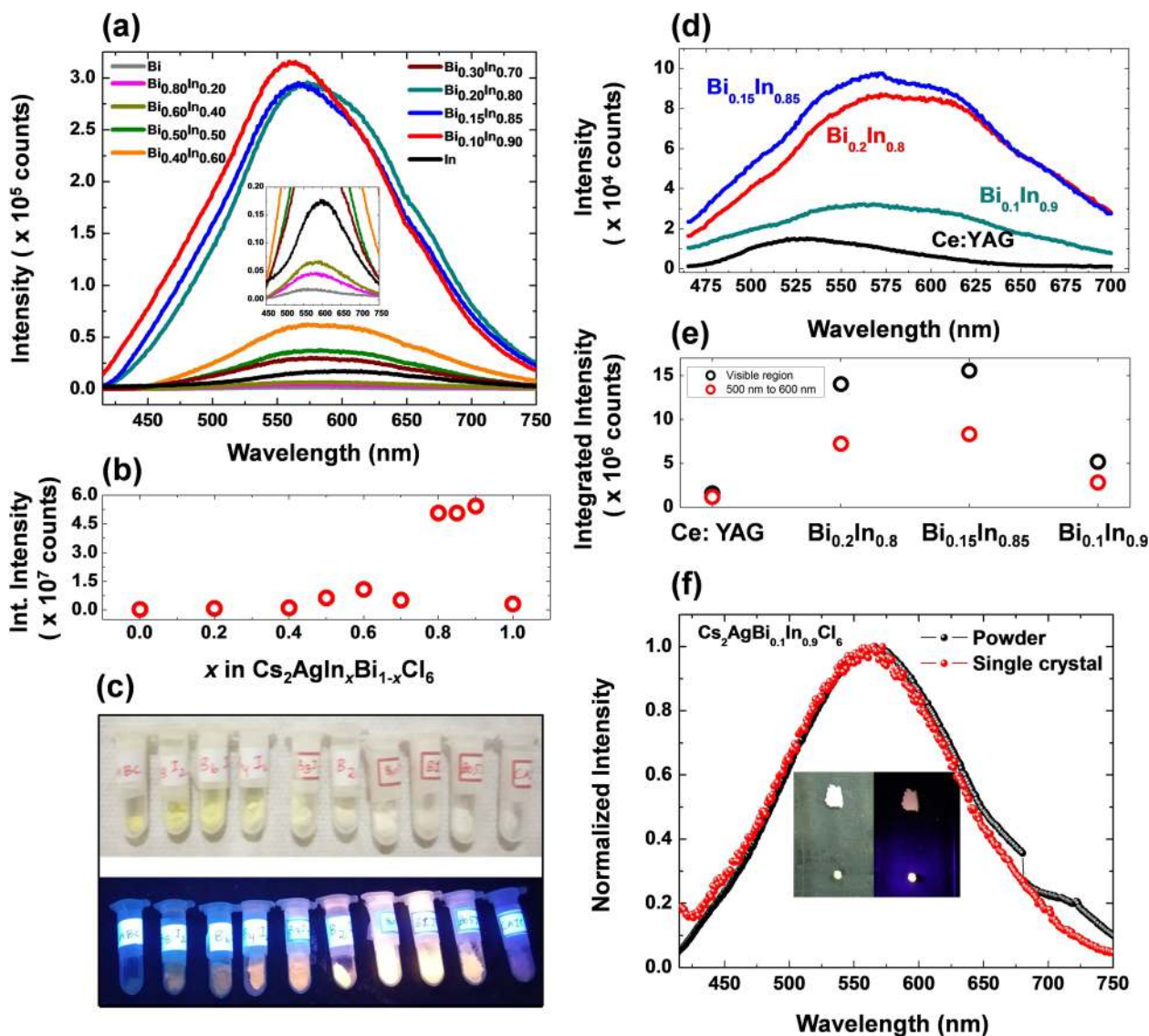


Fig. 3 Photoluminescence properties of $\text{Cs}_2\text{AgIn}_x\text{Bi}_{1-x}\text{Cl}_6$ compounds. **a** Photoluminescence spectra, and **(b)** integrated photoluminescence intensity of $\text{Cs}_2\text{AgIn}_x\text{Bi}_{1-x}\text{Cl}_6$ powders (excitation wavelength-380 nm). Note: The XRD and Raman spectra of the samples with $x = 0.7$ – 0.95 are given in Supplementary Fig. 15 and Supplementary Fig. 16. **c** Photograph of $\text{Cs}_2\text{AgIn}_x\text{Bi}_{1-x}\text{Cl}_6$ compounds, in which the top image shows the samples under room light and bottom images show the samples under 365 nm wavelength UV irradiation. **d** Photoluminescence spectra of Ce:YAG, $\text{Bi}_{0.20}\text{In}_{0.80}$, $\text{Bi}_{0.15}\text{In}_{0.85}$, and $\text{Bi}_{0.10}\text{In}_{0.90}$ compounds excited at 430 nm wavelength for relative quantum yield measurements. **e** Photoluminescence-integrated intensity for Ce:YAG, $\text{Bi}_{0.20}\text{In}_{0.80}$, $\text{Bi}_{0.15}\text{In}_{0.85}$, and $\text{Bi}_{0.10}\text{In}_{0.90}$ compounds, where integrated intensity for covering the entire visible region is given in hollow black circles and integrated intensity for wavelength between 500 and 600 nm is given in hollow red circles. **f** Normalised photoluminescence spectra of $\text{Bi}_{0.10}\text{In}_{0.90}$ compound for a single crystal and powder compounds, where the inset photograph depicts the samples under room light and irradiation at 375 nm wavelength. The crystals are nearly 2 mm in size.

further increases as the x value increases up to 0.9 and drops back. Figure 3c shows the powders under room light and UV illumination, where it is seen very clearly that the samples with $x = 0.8$ and 0.9 show intense white light emission. To make a comparison with the standard white light-emitting materials, we synthesized Ce-doped YAG and compared its photoluminescence with $\text{In}_x\text{Bi}_{1-x}$ ($x = 0.8, 0.85, \text{ and } 0.9$) under given illumination and measurement conditions¹². Figure 3d shows the emission spectra of all these four samples and it can be seen that the mixed trivalent compounds with In^{3+} and Bi^{3+} show much higher emission than the well-known Ce:YAG emitter, with significantly enhanced emission in the red region. The integrated intensity shows that at $x = 0.85$, the light emission of perovskite is 10 times higher than the Ce:YAG. Since the standard material has weak emission in the red region, we also compared the intensity

between 500 and 600 nm, where the perovskite emission is 8.3 times higher than the Ce:YAG (Fig. 3e).

In order to confirm our concept that photoemission does not arise out of defects, we have synthesized a millimeter-sized single-crystal ($x = 0.9$) and carried out emission studies and compared it with the powder sample. The single-crystal also shows broad and intense white light emission (Fig. 3f), like the powders without much shift in peak position². Figure 3f inset shows white light emission by both powders and single crystals.

Power-dependent photoluminescence. To further confirm that the broad emission in the powders does not arise from the surface defects, apart from the photoluminescence on single crystals, power-dependent photoluminescence measurements on powders

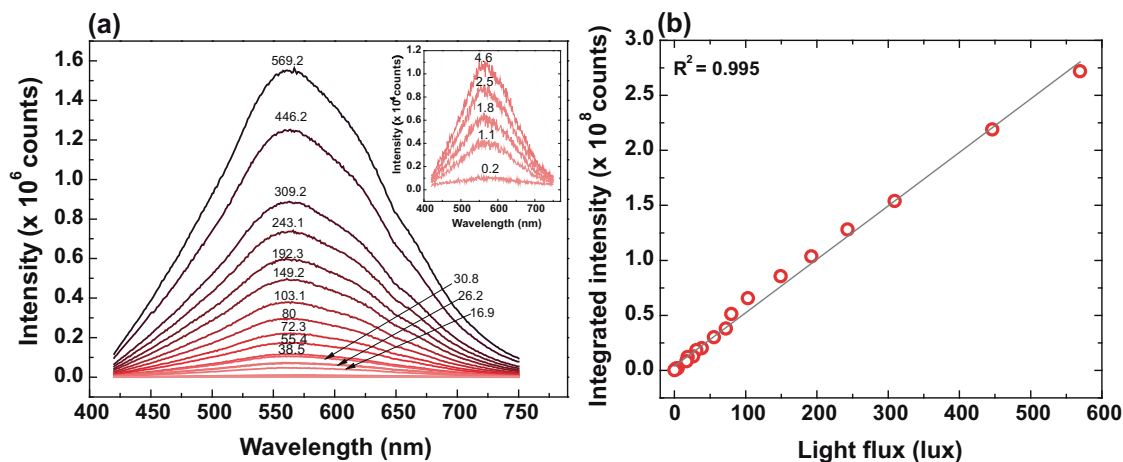


Fig. 4 Power-dependent photoluminescence properties. **a** Power-dependent photoluminescence spectra of $\text{Bi}_{0.10}\text{In}_{0.90}$ compound. The photon flux (380 nm) is varied from 0.2 lux to 569.2 lux. The inset shows the photoluminescence at low photon fluxes (0.2–4.6 lux). **b** The integrated intensity under the photoluminescence curve shown in Fig. 4a is plotted as a function of incident photon flux.

were carried out. The material is excited with 380 nm photons with intensity ranging from 0.2 lux to 570 lux. The photoluminescence plot is shown in Fig. 4a. The integrated intensity under each of the photoluminescence curves is plotted as a function of light flux and the plot is given in Fig. 4b. The integrated intensity varies linearly as the function of incident power. The defect-related emission is expected to give a nonlinear response¹². This result shows that emission does not arise from the defects but possibly due to the band-to-band recombination via self-trapped excitons. The magic composition with $x = 0.8$ – 0.9 where the emission shall arise due to the possibility of the (i) transition from indirect-to-direct bandgap as the x value increases, and/or (ii) change of parity to allow transitions between the valence and conduction band^{5,12}. It is essential to relate these two parameters to the distortion in the structure that can be used as a design principle for future material development.

Investigation on the nature of bandgap. To identify the transition of $\text{Cs}_2\text{AgIn}_x\text{Bi}_{1-x}\text{Cl}_6$ from the direct to the indirect bandgap, we have experimentally studied the excitation spectra at a given photoluminescence emission wavelength. For a direct bandgap semiconductor at any given emission wavelength, the excitation spectra should ideally overlap with the absorption spectrum of the material. For the indirect bandgap semiconductor, no emission can happen from CBM to VBM, as these two are positioned at different symmetry points. But emission can happen at the symmetry point of VBM from the high-energy conduction band positions as shown in Fig. 5a. Essentially, if the onset of the excitation spectrum is the same as the absorption spectrum, it can be assigned as a direct bandgap material, where if its onset wavelength is lower than the absorption onset, it is an indirect bandgap semiconductor. Figure 5b shows the normalized absorption and excitation spectra of samples with various x values. It can be noticed that for CABc, the onset of excitation spectra is at a lower wavelength relative to its absorption onset and it confirms the indirect bandgap nature. But for $x = 1$ (CAIC), the onset of the excitation and absorption is nearly the same and it is a direct bandgap material. When the x is increased from 0 to 1, the difference in the onset decreases and at 0.6, it merges, indicating the transition of the material from indirect to direct bandgap around this x value.

Excited-state photoluminescence properties. The excited-state photoluminescence lifetime was also significantly affected by the

introduction of mixed trivalent systems in the double perovskites. The end member with $x = 0$, that is CABc, upon excitation using 402 nm pulse laser diode (emission monitored at 500 nm), the time taken for 50 % of the excited electrons in the conduction band to decay back to its ground state is nearly 117 ps (Fig. 5c). As the x value increases to 0.6, the lifetime increases further to over 300 ps (Supplementary Fig. 17). But suddenly at $x = 0.8$, more than 3 orders of magnitude increase in the lifetime with nearly 771 ns. An increase in the x value to 0.9, enhanced the lifetime to nearly a μs and at $x = 0.95$, the lifetime suddenly dropped to 390 ns, with the other end member CAIC at $x = 1$ giving the lifetime of few hundreds of ps. Similar to the photoluminescence emission intensity, at x between 0.8 and 0.9, the lifetime suddenly increased by three orders of magnitude, nearing 1 μs half-life decay (Supplementary Table 8). The emission decay of a single-crystal of $\text{Cs}_2\text{AgIn}_x\text{Bi}_{1-x}\text{Cl}_6$ with $x = 0.9$ also has shown 713 ns, which indicates that the high lifetime is not due to traps or defects, rather due to the intrinsic crystal structure of the material (Fig. 5d). Like the emission decay at 500 nm, the photoluminescence emission monitored at 600 nm wavelength also showed a similar trend of a higher lifetime at $x = 0.8$ – 0.9 (Supplementary Fig. 18), indicating that the variation in the lifetime is not wavelength-dependent. The direct bandgap of the material at these magic x values or the parity-allowed transitions, which will be discussed through the band structure analysis that happened due to the Bi^{3+} substitution in In^{3+} , does not explain the increase in the lifetime. The distortion induced in the structure might have created a local polarization that enhances the charge separation efficiency (discussed in the later section)^{48–51}.

Electronic band structure of mixed trivalent perovskites. In the family of halide perovskites, as already been discussed, parity of valence and conduction band edges and the possibility of formation of STE are deterministic for broadband emission. Therefore, here we shall emphasize how parity and STE evolve with mixed 3+ cations. In Fig. 6, we have plotted the band structure of mixed 3+ cationic members $\text{Bi}_{0.25}\text{In}_{0.75}$, $\text{Sb}_{0.25}\text{In}_{0.75}$, and $\text{Sb}_{0.25}\text{Bi}_{0.75}$. The calculated lattice parameters and the bond lengths are given in Supplementary Table 9. In the case of $\text{Bi}_{0.25}\text{In}_{0.75}$, the valence band edge is formed by Ag- e_g orbital character, while the flat conduction band edge is formed by Bi-p orbital character, leading to an even- and odd-parity combination. We may recall that similar was the case for the pristine CABc. However, CABc exhibits the indirect bandgap. In the case

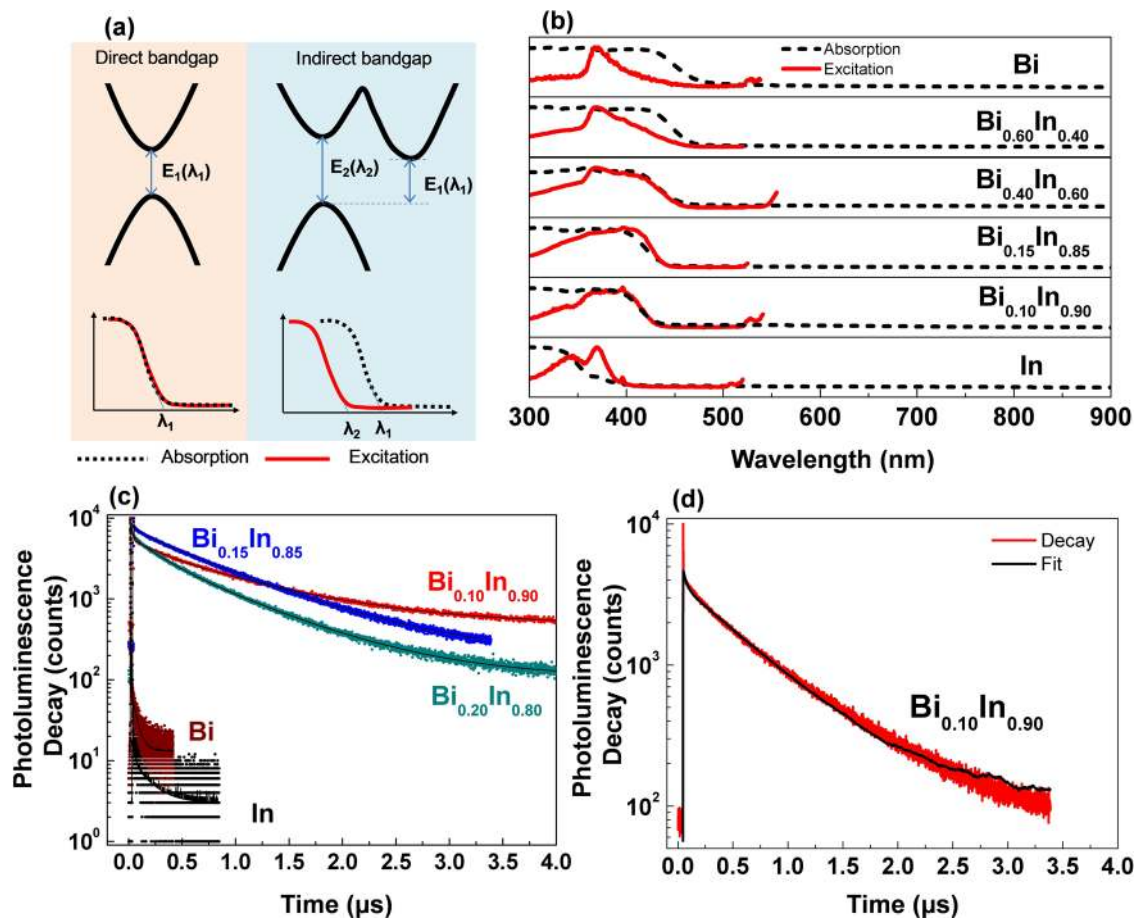


Fig. 5 Excitation and time-resolved photoluminescence properties of halide double perovskites. **a** Schematic representation of direct and indirect bandgap semiconductor materials and their expected absorption and excitation spectra. **b** Normalized absorption and excitation spectra of selected Cs₂AgIn_xBi_{1-x}Cl₆ compounds, where the dotted black line represents the absorption spectra and the solid red line represents the excitation spectra. Excitation spectra were measured by monitoring the emission wavelength at 575 nm. **c** Time-resolved single-photon counting (TRSPC) measurements for CABC, Bi_{0.20}In_{0.80}, Bi_{0.15}In_{0.85}, Bi_{0.10}In_{0.90}, and CAIC compounds. TRSPC measurements were carried out by exciting the samples at a pulsed-laser wavelength of 402 nm and monitored at an emission wavelength of 500 nm (solid circles represent the photoluminescence decay and the solid black line represents the fitted components). **d** Time-resolved photoluminescence spectrum of single-crystal Bi_{0.10}In_{0.90} sample at emission wavelength 500 nm.

of pristine CAIC, which exhibits a direct bandgap, the conduction band edge is formed by In-s, making it even-even parity. Furthermore, the pristine CAIC shows a flat valence band along the path Γ -X, which is also inherited by the mixed 3+ cationic system. Collectively the mixed cationic compound has both even-odd combinations to facilitate optical transition and possibility of formation of STE to create broadband emission²⁸. Our experimental studies show that white light emission occurs when In is present in the range of 0.7 to 0.9, which is in agreement with this theoretical inference. We have shown the $x = 0.5$ (Supplementary Fig. 19) band structure, which shows a dispersive band feature as well as indirect bandgap nature.

Like the case of Bi_{0.25}In_{0.75}, the compound Sb_{0.25}In_{0.75} also exhibits the direct bandgap of 2.7 eV. However, in this case, the conduction band edge is a combination of Sb-p and In-s orbitals. The CBM occurs at Γ and eigenfunction here is of even parity (Fig. 6) as In-s orbital character populates over Sb-p, and VBM is a linear combination of Ag-e_g inherited from pristine compounds and the valence band edge is predominantly made of Sb-s character throughout the Brillouin zone. Thus, the transitions, in this case, are forbidden due to even-even parity. This agrees well with the experimental studies where only a weak emission is observed (Supplementary Fig. 14). This disparity comes due to a change in the CBM position. We observed that the CBM position

is highly sensitive to the M (M')-X bond length. A change in M (M')-X bond length shifts the CBM to X, where the conduction band edge parity is odd to allow the transitions. In the case of Sb_{0.25}Bi_{0.75}, though VBM and CBM have opposite parity, however, the bands retain their dispersive and indirect bandgap nature, similar to their pristine form and due to high electronic dimensionality, the broadband emission is not favored.

Electric-bias-dependent photoluminescence properties. In some of the recent reports, the effect of pressure on the structure and subsequently the photoluminescence was reported^{25,28,29,52}. The distorted crystal structure influenced both the intensity and the spectral range of emission. Here in this paper, we reported the chemical distortion of the crystal by introducing a mixed trivalent state in the M site, which distorts the [AgCl₆]⁵⁻ octahedra, subsequently leading to the change in the optical properties. To prove that distortion in the material is playing a role in the emission properties, we intentionally created the distortion by applying external electric bias in the symmetric CAIC and CABC structures and also made similar studies in already-distorted Cs₂AgIn_{0.9}Bi_{0.1}Cl₆⁵³.

Thin pellets of these materials were held between fluorine-doped tin oxide-conducting glasses and a sequence of potentials are applied: 100 V for 5 min, 200 V for 5 min, and 300 V for 5, 10, 60, and 90 min,

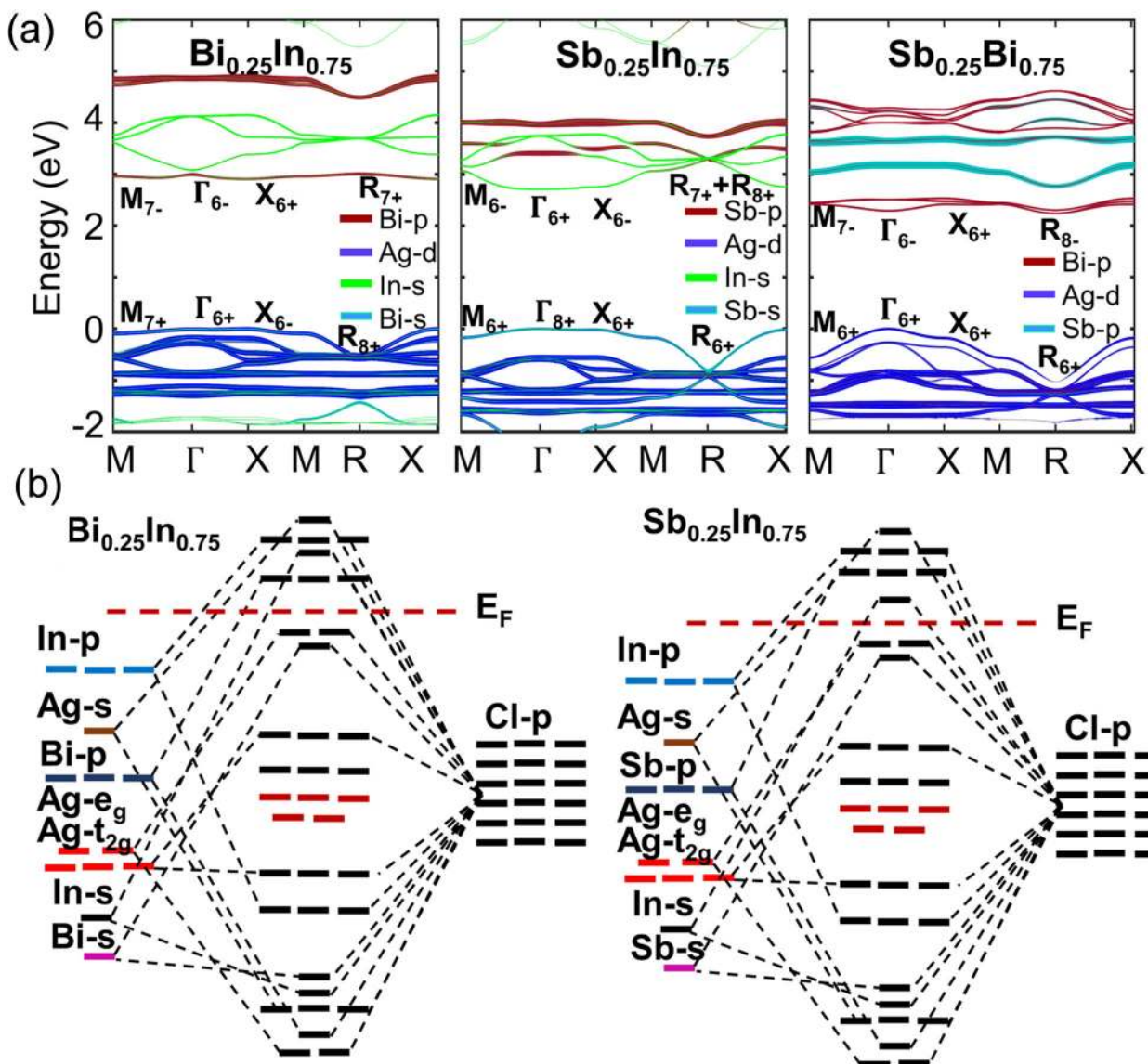


Fig. 6 Band structure of mixed trivalent halide double perovskites. **a** Band structure of mixed $\text{Cs}_2\text{AgBi}_{0.25}\text{In}_{0.75}\text{Cl}_6$, $\text{Cs}_2\text{AgSb}_{0.25}\text{In}_{0.75}\text{Cl}_6$, and $\text{Cs}_2\text{AgSb}_{0.25}\text{Bi}_{0.75}\text{Cl}_6$ double perovskites with dominant orbital characters and parities of eigenfunctions in terms of Koster notations at valence and conduction band edges. **b** Molecular orbital picture of mixed $\text{Cs}_2\text{AgBi}_{1-x}\text{In}_x\text{Cl}_6$ and $\text{Cs}_2\text{AgSb}_{1-x}\text{In}_x\text{Cl}_6$ double perovskites obtained from the analysis of orbital resolved bands and density of states.

and photoluminescence measurements are taken after every step in the sequence. Similarly, after turning off the external bias, at least four photoluminescence measurements were taken over a period of 80 min (Fig. 7). Upon the application of the electric bias, the emission is constantly increased for CABC, and upon turning the bias off, the emission tends to decrease back again. For CABC, the emission intensity after the complete bias sequence is 1.25 times higher than the material before bias. The CAIC, that is at $x = 1$, upon bias, shows two different phenomena: one, the emission spectra shifted to red, and initially, the emission intensity decreased drastically, followed by a rise. At the application of 100 V, a nearly 35% decrease in the intensity is observed, followed by a rise, during the other sequence of voltages. Upon turning off the voltage bias, the emission decayed back to the value at 100 V. It has to be noticed that emission is increased nearly 25% for the case of CABC upon the application of electric bias, whereas no net emission change is observed at the end of the bias sequence, in CAIC. For a sample with $x = 0.9$, to a greater surprise, the emission remained perfectly constant over the entire sequence of voltage bias. This indicates that a material that is already distorted

chemically cannot be distorted further, whereas the end members that are perfectly symmetric, upon the application of the bias, a probable distortion happened, which leads to a change in the photoluminescence emission²⁴. The integrated area during/after bias normalized to photoluminescence before applying the bias is shown in Fig. 8 and Supplementary Fig. 20.

The application of bias did not degrade the structure, as evident from the PXRD pattern shown in Supplementary Fig. 21 and Supplementary Fig. 22. The patterns remain the same with no formation of new peaks; however, a shift in the peak position to higher angles is observed for CAIC upon applied bias, indicating the possible contraction between planes. The lattice parameter of the CAIC pellet decreased from 10.472 Å to 10.468 Å. Unlike the CAIC case, the PXRD taken before and after the bias for $x = 0.9$, did not show any change in the peak positions. Since the latter material is chemically distorted, no further distortion seems possible with the application of electric bias. From these bias-dependent studies, it is very clear that distortion is playing a significant role in the emission properties of the materials.

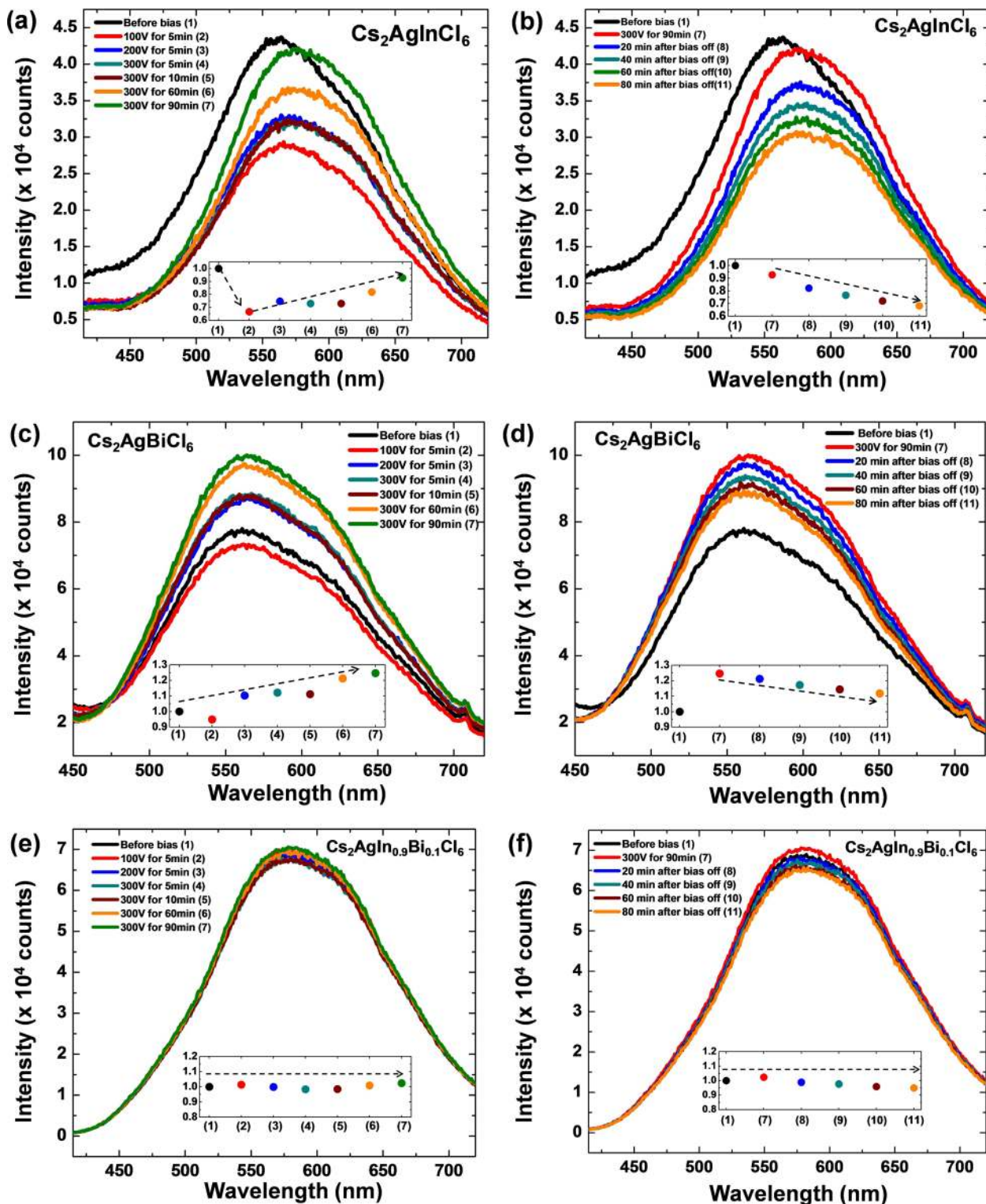


Fig. 7 Electric-bias-dependent photoluminescence properties. Photoluminescence spectra of (a, b) $\text{Cs}_2\text{AgInCl}_6$, (c, d) $\text{Cs}_2\text{AgBiCl}_6$, and (e, f) $\text{Cs}_2\text{AgIn}_{0.9}\text{Bi}_{0.1}\text{Cl}_6$. The inset shows the integrated intensity of photoluminescence curves at various measurement conditions. Plots (a, c, and e) show the spectra of compounds under various applied voltages at different times. The inset shows the integrated intensity of photoluminescence curves at various measurement conditions. Plots (b, d, and f) show the spectra at different intervals after switching off the voltage bias.

Structural distortion analysis using far-IR absorption.

Although CAIC shows a decrease in the lattice parameter, it does not provide information on the structural changes. So, to further understand the structural distortion induced in the material due to mixed trivalent substitution or the application of the electric bias,

FTIR measurements were carried out. Any symmetric octahedra system possesses six different vibration modes and two (T_{1u} stretching (s) and T_{1u} bending (b)) of them are IR active⁵⁴. In the double perovskites under study, there are two different octahedra [AgCl_6]⁵⁻ and [M^{3+}Cl_6]³⁻. So in the FTIR spectra, it is expected

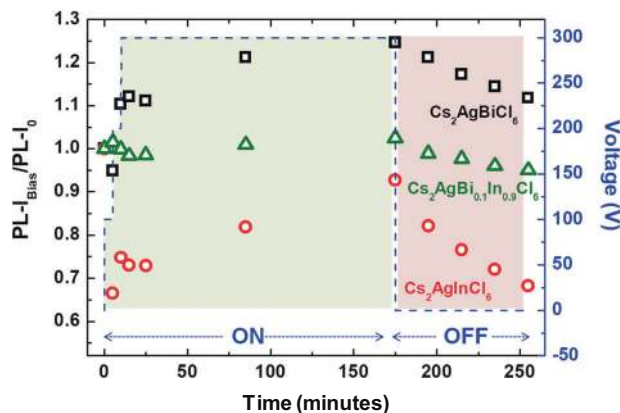


Fig. 8 Bias-dependent emission spectra. Ratio of integrated photoluminescence intensity measured under biased voltages to photoluminescence intensity measured before applied voltage as the function of time is plotted for CAIC, CABC, and $\text{Bi}_{0.10}\text{In}_{0.90}$ compounds. The void black-colored squares represent the CABC, void green-colored triangle represents the $\text{Bi}_{0.10}\text{In}_{0.90}$, and void red-colored circle represents the CAIC compounds.

to have four absorption peaks. Figure 9 shows the FTIR spectra of $\text{Cs}_2\text{AgInCl}_6$, $\text{Cs}_2\text{AgBiCl}_6$, and the mixed trivalent compound. The indium containing sample has four distinct peaks: 249 cm^{-1} (s), 134 cm^{-1} (b), 73 cm^{-1} (s), and 60 cm^{-1} (b). The former two correspond to the vibrational modes of $[\text{InCl}_6]^{3-}$ and the latter two correspond to $[\text{AgCl}_6]^{5-}$. The bismuth-containing sample also has four peaks 158 cm^{-1} (s), 103 cm^{-1} (b), 70 cm^{-1} (s), and 56 cm^{-1} (b). Similar to $\text{Cs}_2\text{AgInCl}_6$, the two peaks at higher wavenumbers correspond to $[\text{BiCl}_6]^{3-}$ and the latter two belong to $[\text{AgCl}_6]^{5-}$. The zoomed-in version of $[\text{AgCl}_6]^{5-}$ is given in Fig. 9b. Apart from the peak positions, one of the key observations is that the stretching vibrational modes of the $[\text{BiCl}_6]^{3-}$ octahedra are very broad. The broad peak is expected to arise due to the presence of an inert electron pair in the valence 6s orbitals in Bi^{3+} . Although chemically only six coordinations exist, the lone pair orbitals act as a seventh coordination site and induce distortion. This distortion led to the observation of wide absorption peaks for $[\text{BiCl}_6]^{3-}$. Similarly, an inert electron pair also exists for Sb^{3+} and a broad stretching peak is observed in $\text{Cs}_2\text{AgSbCl}_6$ (Supplementary Fig. 23)^{55–57}.

The presence of mixed trivalent cations (Bi^{3+} and In^{3+}) shows distortion in the $[\text{AgCl}_6]^{5-}$ octahedra, which is confirmed by single-crystal XRD. If an asymmetry is introduced in a compound reducing the point group symmetry from O_h to C_{3v} or lower, the stretching and bending peaks are expected to split. In the presence of mixed Bi^{3+} and In^{3+} , we have observed the split in the stretching modes (denoted by dotted arrows at 72 and 64 cm^{-1} in Fig. 9b). The bending-mode onset appears at lower frequencies compared with the end members and the peak is expected below 50 cm^{-1} .

Similarly, to confirm the distortion due to the applied electric field, FTIR measurements were carried out on pellets: (i) pressed from the respective double-perovskite powders under mild applied pressure, (ii) immediately after the application of electric bias (90 min, 150 V), and (iii) after 90 min bias followed by 90 min of rest (Fig. 9c–f). The application of pressure to make the pellet in $\text{Cs}_2\text{AgBiCl}_6$, narrowed the stretching vibrational peak of $[\text{BiCl}_6]^{3-}$ and introduced a split of 5 cm^{-1} in $[\text{AgCl}_6]^{5-}$ stretching mode. The bending-mode onset is shifted to lower wavenumbers, similar to the observations in Fig. 9b. The application of pressure in $\text{Cs}_2\text{AgInCl}_6$ broadened both the bending and stretching modes of $[\text{InCl}_6]^{3-}$ and also shifted the

peaks to lower wavenumbers. The $[\text{AgCl}_6]^{5-}$ peaks in the latter compound become narrow, unlike $\text{Cs}_2\text{AgBiCl}_6$, and shifted to lower wavenumbers. The onset of the bending mode is observed near 60 cm^{-1} and its peak is expected below 50 cm^{-1} .

The application of the electric field to $\text{Cs}_2\text{AgBiCl}_6$ pellet further narrowed the stretching peaks of $[\text{BiCl}_6]^{3-}$, and also introduced a significant split in the stretching peaks of $[\text{AgCl}_6]^{5-}$. The difference between the bending peaks increased from 5 cm^{-1} to 10 cm^{-1} upon the application of bias (Fig. 9d). However, after 90 min of rest, the difference reduced back to approximately 5 cm^{-1} . So, the split in peaks shall be attributed to the decrease in the symmetry of $[\text{AgCl}_6]^{5-}$ octahedra and it is similar to the observations in $\text{Cs}_2\text{AgIn}_x\text{Bi}_{1-x}\text{Cl}_6$ (Fig. 9b). This result indicates that both by the mixed trivalent substitution and by the application of the electric field, the asymmetry shall be introduced in the double perovskite. It has to be noted that application of the electric field modified the symmetry of both the $[\text{BiCl}_6]^{3-}$ and $[\text{AgCl}_6]^{5-}$ octahedra; however, the mixed trivalent substitution selectively introduced distortion in $[\text{AgCl}_6]^{5-}$.

The application of the electric field in $\text{Cs}_2\text{AgInCl}_6$ introduced a lot of small vibrations peaks between 300 and 70 cm^{-1} and it might be due to the introduction of significant asymmetry in the octahedron formed by $[\text{InCl}_6]^{3-}$. Some of the new peaks introduced are highlighted in Fig. 9f. $[\text{AgCl}_6]^{5-}$ peak showed only a little change upon the application of electric bias. The IR spectra taken after 90 min of rest tend to reduce the intensity of the new peaks introduced by bias. Like $\text{Cs}_2\text{AgBiCl}_6$, the latter material also tends to go back to equilibrium after removing the electric field. From the variation in the FTIR signatures of $[\text{AgCl}_6]^{5-}$ and $[\text{M}^{3+}\text{Cl}_6]^{3-}$, it can be suggested that the application of electric bias distorted both the trivalent and monovalent metal-containing octahedra in $\text{Cs}_2\text{AgBiCl}_6$, whereas only the trivalent metal-containing octahedra are distorted in $\text{Cs}_2\text{AgInCl}_6$. The mixed trivalent chemical substitution introduced asymmetry only in the $[\text{AgCl}_6]^{5-}$ octahedra, whereas the application of the electric field can introduce distortion in either the $[\text{M}^{3+}\text{Cl}_6]^{3-}$ or $[\text{AgCl}_6]^{5-}$ or both the octahedra.

Electric-bias-dependent excitation spectra. The chemically induced distortion influenced the emission by changing the parity in the electron transitions from the valence band to the conduction band. In typical absorption spectra, change of parity is expected to increase the extinction coefficient, as dictated by Beer–Lambert’s law⁵. This should also be reflected in the excitation spectra since the latter monitors the wavelength of absorbed photons that is responsible for the emission. To confirm this phenomenon, we carried out electric-bias-dependent excitation spectra, where three measurements were made, one before electric bias, the second and last one after the application of 300 V for 5 min and 90 min, respectively. For CABC (Fig. 10a), the intensity of excitation spectra increased over the application of 300 V bias for 5 min and 90 min. Whereas, for CAIC (Fig. 10b), initially the excitation intensity decreases, followed by an increase. In the case of the sample with $x = 0.9$ (Fig. 10c), literally no change in the intensity is observed. These results are in line with the bias-dependent emission measurements. As the thickness of the sample, illumination area, and all the other measurement parameters are kept constant, the change in the excitation spectra intensity shall be attributed only to the change in the extinction coefficient, which is in line with the distortion-induced emission data shown in Fig. 3a. Chemically induced distortion, due to the mixed trivalent cation, introduced a change in the parity from forbidden to allowed transition leading to an increase in the emission. Similarly, from the excitation results, it can be suggested that a change in the parity might be responsible for the increase in the excitation intensity

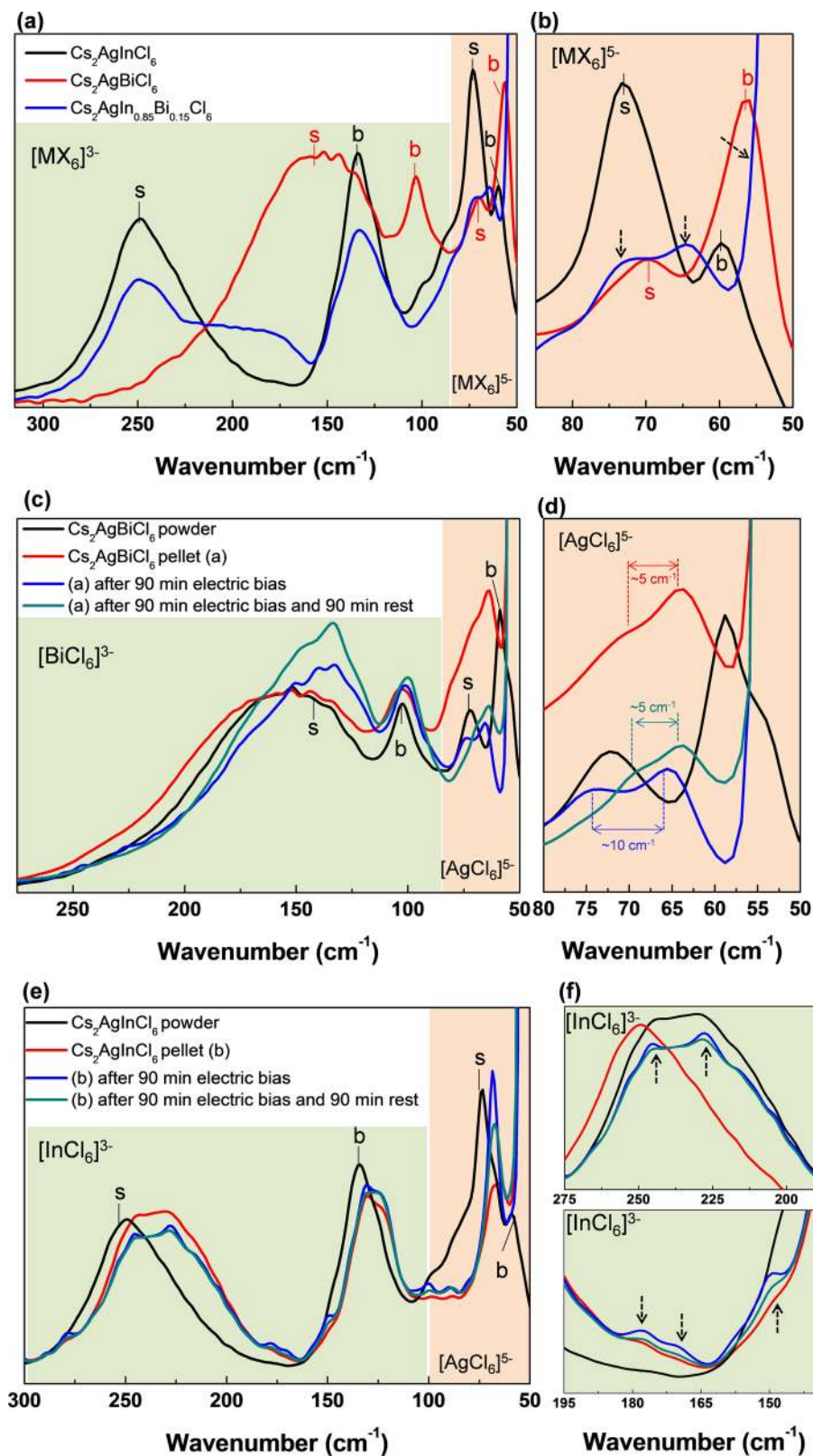


Fig. 9 FTIR spectra of halide double perovskites. **a, b** $\text{Cs}_2\text{AgBiCl}_6$, $\text{Cs}_2\text{AgInCl}_6$, and $\text{Cs}_2\text{AgIn}_{0.85}\text{Bi}_{0.15}\text{Cl}_6$ powders. **c, d** The spectra of CABP powders and pellet before and after the application of electric bias. **e, f** The spectra of CAIC powders and pellet before and after the application of electric bias.

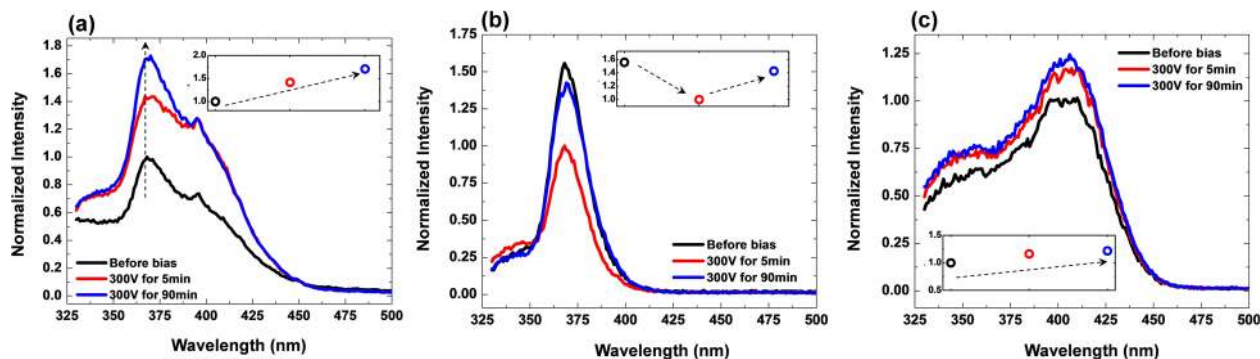


Fig. 10 Bias-dependent excitation spectra. Excitation spectra of (a) CABC, (b) CAIC and, (c) $\text{Bi}_{0.10}\text{In}_{0.90}$ compound measured at an applied voltage of 300 V. Here, excitation spectra monitored at an emission wavelength of 575 nm.

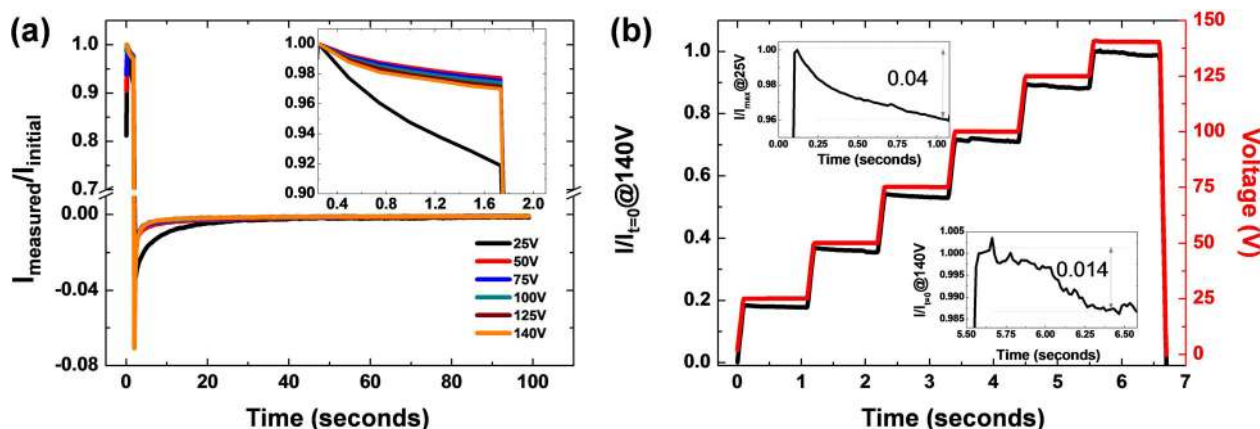


Fig. 11 Polarization measurements for $\text{Cs}_2\text{AgIn}_{0.9}\text{Bi}_{0.1}\text{Cl}_6$. **a** Pulse-voltage measurement: Voltage V applied for 2 s followed by 0 V for 100 s and current is monitored during this entire duration. Y-axis shows the ratio of the current measured during the scan to the initial current (immediately right after applying the bias) measured at the corresponding applied voltages. The inset shows the zoomed-in plot of the first 2 s. **b** Staircase-voltage measurement: a step voltage in multiples of 25 V is applied for 1 s each and current is monitored over the entire time duration. Y-axis (including insets) provides the ratio of maximum current to the measured current over the entire duration. The inset shows the zoomed-in version at 25 and 140 V.

upon the application of the electric field for CAIC and CABC. No bias-dependent changes for a sample with $x = 0.9$, indicate that the distortion in the $[\text{AgCl}_6]^{5-}$ octahedra introduced by mixed trivalent cations is probably far higher than the application of electric bias. The $\text{In}_x\text{Bi}_{1-x}$ with x between 0.8 and 0.9 shows very high emission intensity and from the DFT, bias-dependent emission and excitation studies, it is clear that the change in the parity for allowed optical transition introduced by the $[\text{AgCl}_6]^{5-}$ octahedral distortion is responsible for intense white light emission. However, the increase in the excited-state lifetime by more than two orders of magnitude shall not be explained by the change in the parity, but the role of polarization due to the crystal structure shall be responsible.

Polarization in halide double perovskites. All the material synthesized with varying x values crystallized in the centrosymmetric space group, so this rules out the concept of ferroelectric polarization. However, there is a possibility of local dielectric polarization due to the distortion in the $[\text{AgCl}_6]^{5-}$ octahedra. We first carried out P-E loop measurement for the sample with $x = 0, 0.9$, and 1. All the three samples at sufficiently low switching frequencies displayed ellipse-shaped curves indicating the resistive loop (Supplementary Fig. 24 to Supplementary Fig. 26). A typical loop will have its contribution from both DC conduction and polarization currents. If the material is sufficiently conductive, the leakage current due to DC conduction will dominate

the loop behavior, which is the case with most of the halide perovskites⁵⁸. The conventional ferroelectric semiconductor, BiFeO_3 , also shows leakage current and traditionally it can be deconvoluted using (i) staircase voltage or (ii) single-voltage pulse techniques while monitoring the current as a function of time. In the staircase/pulse-voltage studies, upon voltage bias, the initial current response, in the first few ms, will be a sum of DC plus polarization currents, whereas after the material is completely polarized, only DC current will be observed. As polarization is a fast phenomenon, subtracting the peak current observed at the first few ms, from the steady-state current at longer timescales can provide information on the polarization currents. In the case of the pulse-voltage technique, additional information can be obtained by monitoring the reverse current after the voltage is turned off. This reverse current is reminiscent of depolarization. The area under the reverse current will give an indication of the polarization current^{59–61}.

We carried out pulse-voltage measurement where a voltage V is applied for 2 s followed by 0 V for 100 s and the current is monitored during the entire duration. For the sample $x = 0.9$, during the pulse, steady-state current is reached between 97% and 98% of the peak current. This implies that nearly 2–3% of the current arises from the polarization (Fig. 11a). When the pulse voltage is turned off, a reverse current flow is observed, but it remained fairly constant at various applied voltage (except for 25 V). This implies that the depolarization current is constant and it indicates the application of bias is not inducing any fresh

polarization. Similar to pulse measurements, we have carried out staircase voltage measurements by applying a voltage in multiples of 25 V up to 150 V, 1 s each, and the current is monitored over time. Like in pulse measurements, the polarization current (peak current-steady-state current) at various applied voltages remains nearly the same between 1.5 and 4% (Fig. 11b). In the case of CAIC or CAB, no steady-state current value is reached at various applied voltages, during the measurement duration with both the pulse (Supplementary Fig. 27, Supplementary Fig. 28) and staircase (Supplementary Fig. 29, Supplementary Fig. 30) techniques. In fact, at voltages beyond 50 V, the current constantly kept increasing as a function of time, unlike the mixed trivalent compound where the steady-state is reached. We believe that the application of electric bias in CAIC and CAB is inducing continuous movement of ions during the entire measurement duration, resulting in unsteady-state current. Further studies on pulse or staircase voltage measurements at very slow time scales, in the order of hours to reach a steady-state, are required, in order to quantify the polarization of the end members. These results are in line with the variation in the emission properties where the photoluminescence varied for end members but remained constant for $\text{Cs}_2\text{AgIn}_{0.9}\text{Bi}_{0.1}\text{Cl}_6$. The structural distortion induces the changes in the parity as well as creates local polarization, leading to enhanced photoluminescence emission yield and higher excited-state lifetime. The distortion can be induced chemically by using mixed trivalent cations or by applying electric bias. The distortion induced due to the application of electric bias did not affect the excited lifetime significantly in both CAIC and CAB. More details are given in Supplementary Fig. 31.

Conclusion

In this paper, we have clearly proved the role of distortion, created either via chemical methods by using mixed trivalent cations or by electric bias, in the photoluminescence properties. We incorporated a strategy of using mixed trivalent cations so as to introduce distortion in $[\text{AgCl}_6]^{5-}$ octahedron. Although distortion is induced in both $\text{Cs}_2\text{AgIn}_x\text{Bi}_{1-x}\text{Cl}_6$ and $\text{Cs}_2\text{AgBi}_x\text{Sb}_{1-x}\text{Cl}_6$, due to the indirect bandgap nature of the material or parity-forbidden transitions, the latter compounds do not show emission. Whereas among the mixture of In^{3+} and Bi^{3+} , the direct bandgap is observed for samples with x over 0.5 and the creation of parity allowed transitions for x between 0.8 and 0.9, making them highly photoluminescent. With the help of staircase and pulse-voltage measurement, the possibility of the presence of the polarization due to the distortion is confirmed. This polarization led to effective charge separation with a near-microsecond excited state lifetime. This work can potentially harness the interest of material scientists to design and synthesize materials that possess distortion in the octahedron for a higher quantum yield in LEDs. The bottom line to create highly fluorescent halide perovskite is to introduce distortion in the MCl_6 octahedron while retaining the direct bandgap and parity-allowed transitions in the material. In addition to light-emitting application, the higher excited lifetime in distorted materials can lead to highly efficient photo- or photoelectrocatalytic solar fuel systems, including water splitting and carbon dioxide reduction.

Methods

Chemicals used. Cesium chloride (CsCl , 99.9%), silver chloride (AgCl , 99.9%), bismuth trichloride (BiCl_3 , 99.9%), indium trichloride (InCl_3 , 99.9%), and antimony trichloride (SbCl_3 , 99.9%), were purchased from Alfa Aesar. Hydrochloric acid and isopropyl alcohol were purchased from Rankem Company. All chemicals were used without any further purification.

Synthesis of halide double-perovskite compounds. $\text{Cs}_2\text{AgBiCl}_6$ powders were synthesized by hydrothermal method using CsCl , AgCl , and BiCl_3 salts in 2:1:1 mol. ratio dissolved in 10 M hydrochloric acid. The precursor solutions were carefully transferred and sealed in 30 ml Teflon-lined stainless-steel autoclave and kept in an oven at 180 °C for 12 h. The light-green color material obtained was filtered with Sartorius filter paper and finally washed with isopropyl alcohol for few times and dried in a hot air oven at 80 °C for 12 h. The $\text{Cs}_2\text{AgSbCl}_6$ and $\text{Cs}_2\text{AgInCl}_6$ powders were prepared by a similar procedure mentioned above where BiCl_3 was replaced by SbCl_3 and InCl_3 , respectively. For mixed trivalent compounds of halide double perovskites $\text{Cs}_2\text{AgIn}_x\text{Bi}_{1-x}\text{Cl}_6$, BiCl_3 , and InCl_3 precursors were used in the respective proportions. Similarly for the antimony substitution, $\text{Cs}_2\text{AgIn}_x\text{Sb}_{1-x}\text{Cl}_6$ and $\text{Cs}_2\text{AgBi}_x\text{Sb}_{1-x}\text{Cl}_6$ powders are achieved by taking appropriate mole fractions of In/Sb or Bi/Sb salts.

Synthesis of single-crystal halide double perovskites. To synthesize single-crystals halide double-perovskite compounds, an experimental procedure similar to powder synthesis was followed but with slight modification in the cooling process after the hydrothermal process at 180 °C for 12 h. The samples were slowly cooled down to 60 °C over a period of 48 h.

Ce^{3+} doped $\text{Y}_3\text{Al}_5\text{O}_{12}$ (Ce:YAG) synthesis. Ce:YAG powders were synthesized by coprecipitation method following the procedure given in a literature report⁶². For synthesis, $\text{Y}(\text{NO}_3)_3 \cdot 6\text{H}_2\text{O}$, $\text{Al}(\text{NO}_3)_3 \cdot 9\text{H}_2\text{O}$, and $\text{Ce}(\text{NO}_3)_3 \cdot 6\text{H}_2\text{O}$ were taken in a stoichiometric ratio of 2.997:5:0.003, respectively, and dissolved in distilled water. Then ammonia solution of 5 M was added dropwise into the mixed solution until pH turns 8.5 and the precipitates were formed, which were filtered and washed with distilled water and ethanol for many times. The washed precipitate was dried at 80 °C for 12 h and annealed at 1000 °C for 4 h. White crystalline Ce:YAG powders were obtained. For Ce:YAG, photoluminescence spectra were carried out to compare with halide double-perovskite compounds. An excitation wavelength of 430 nm was used to measure the emission spectra of Ce:YAG, and selected samples of $\text{Cs}_2\text{AgIn}_x\text{Bi}_{1-x}\text{Cl}_6$ compounds.

Structural characterization. The crystalline structure and phase identification were performed by X-ray diffraction techniques. For single-crystal compounds, X-ray diffraction measurements were carried out at 200 K by using Bruker D8 VENTURE single-crystal X-ray diffractometer equipped with Mo K α X-ray source of wavelength 0.71073 Å and a PHOTON 100 CMOS detector. The grown crystals were mounted on a Kapton loop, where crystals have been coated with paratone-N oil. Data reduction and absorption correction were done using the stand-alone programs, SAINT and SADABS from Bruker, respectively. The collected data were refined using WINGX-SHELX software and then a CIF check was carried out using the service of IUCR.

For powders of $\text{Cs}_2\text{AgIn}_x\text{Bi}_{1-x}\text{Cl}_6$, powder XRD measurements were performed with the help of Rigaku using Cu-K α source of wavelength 1.5406 Å in the region $2\theta = 10^\circ$ – 60° with the step size of 0.02°. For $\text{Cs}_2\text{AgIn}_x\text{Sb}_{1-x}\text{Cl}_6$ and $\text{Cs}_2\text{AgBi}_x\text{Sb}_{1-x}\text{Cl}_6$ samples, X-ray diffractions were carried out by D8 Advance, Bruker using Cu-K α source. Raman spectroscopy techniques were collected either with (i) confocal Raman spectrometer equipped with Nd:YAG laser of 532 nm excitation wavelength using WITec alpha 300 Confocal Raman System or (ii) a handheld BWTEK NanoRam with 785 nm laser excitation. FTIR measurements were carried out using JASCO 6600FV spectrometer fitted with an ATR setup. The spectrometer was operated in complete vacuum for far-IR measurements. Voltage-dependent FTIR measurements were carried out using a compact pellet of CAB and CAIC samples. The voltage (150 V) is applied using a DC power supply for 90 min.

Optical measurements. The absorption measurements of powder samples were collected using Shimadzu 2600 spectrometer equipped with a barium sulfate-coated integrating sphere. Steady-state photoluminescence measurements were performed using Horiba Fluorolog Spectrofluorometer (Fluorolog-3) containing a 450 W xenon arc lamp with double-excitation monochromator and a single-emission monochromator. A photomultiplier tube detector is used to monitor the photons from the emission monochromator. Emission spectra of samples were carried out by exciting at either 370 nm or 380 nm. To eliminate second-order photons, appropriate long-pass cut-off filters were used at the entry port of the emission monochromator. For powders, the perovskite samples were smeared onto optical-quality quartz glass and the illumination area was kept constant for all the samples. For a single-crystal, samples were loaded in a quartz cuvette and emission spectra were measured under the same excitation/filter conditions. The excitation spectra were carried out in Fluorolog-3, where the emission monochromator was set at 575 nm and the excitation spectra were recorded between 300 and 540 nm with a 550 nm long pass cut-off filter. For the power-dependent photoluminescence measurements, the intensity of the incident photons is controlled by using a range of neutral density filters at the exit port of the excitation double monochromator.

Lifetime measurements were collected using the same equipment with a 402 nm NanoLED laser diode that can give a pulse width of less than 200 ns. The obtained data were fitted by Datastation software.

Voltage-dependent photoluminescence spectra. As synthesized samples were grinded into fine powder using pestle–mortar and a compact pellet was pressed using hydraulic press onto an 8 mm diameter die for 8 min. Then pellet was kept in between two cleaned fluorine-doped tin oxide conducting glasses, which are wired with DC power supply and then fixed to a sample holder in Fluorolog-3 spectrofluorometer. For emission spectra measurements, voltage was applied to the samples for the known time using a Delta Elektronika (ES 0300-0.45) DC power supply. The emission spectra were measured immediately after turning off the power supply. For voltage-dependent excitation spectra, similar procedures of sample preparation have been carried out and then measured the excitation spectra.

Polarization studies. The P-E loop, step, and staircase polarization measurements were carried out from the pellets of the corresponding materials using aixACCT TF3000 Analyzer fitted with a 150 V amplifier.

Computational details. The electronic structure calculations of the considered double-perovskite compounds are carried out using density functional theory (DFT) through a full-potential linearized augmented plane-wave (FP-LAPW) method as implemented in the WIEN2k simulation package⁴⁴. The generalized gradient approximation (through PBE formalism) combined with modified Becke–Johnson (mBJ) potential is used for the description of exchange–correlation potentials⁶³. The basis set, employed for the SCF calculations, consists of augmented plane waves occupying the interstitial region and localized orbitals (Cs-6s, Bi-6s, 6p), Sb-5s, 5p), Ag-4d, In-5s, 5p) and Cl-5p) occupying the respective muffin-tin spheres $R_{MT}^{Cs} = 2.5$ a.u., $R_{MT}^{Bi} = 2.5$ a.u., $R_{MT}^{Sb} = 2.5$ a.u., $R_{MT}^{Cl} = 2.27$ a.u., $R_{MT}^{In} = 2.5$ a.u. The number of plane waves is determined by setting to $R_{MT}K_{MAX} = 7.0$. The Brillouin zone integration is carried out with a Monkhorst-Pack grid. We used a k-mesh of $14 \times 14 \times 14$ (yielding 104 irreducible points) for the ground-state structure and $8 \times 8 \times 8$ (yielding 35 irreducible points) for alloyed structure. The structural optimization is carried out using VASP code within the frame of GGA-based PBE functional, to obtain lattice parameters and atomic positions of the pure as well as alloyed compounds⁶⁴. The cut-off energy for basis functions was 500 eV and all the atoms were relaxed until the Hellmann–Feynman forces on them were below 0.001 eVÅ⁻¹. The lattice parameter and various bond lengths of the pure and alloyed compounds are listed in Supplementary Table 1.

The MOP is constructed in three steps. In step 1, the free atomic energy eigenvalues of the participating orbitals, which are already calculated through Hartree–Fock theory and are available in the database, are considered as on-site energy or initial position. In step 2, the orbital-resolved band structures of the compounds, calculated using DFT, are then analysed to understand the nature of chemical bonding and thereby the strength of this bonding. The latter is estimated from the respective bandwidths and separation of the states. In step 3, both step 1 and step 2 are collectively considered to draw the MOP. The tentative position of the Fermi level is determined by occupied and unoccupied states.

Data availability

The Crystallographic Information Files (CIF) reported in this study have been deposited at the Cambridge Crystallographic Data Centre (CCDC), under deposition numbers 2043336-2043341. These data can be obtained free of charge from the Cambridge Crystallographic Data Centre via www.ccdc.cam.ac.uk/data_request/cif. All other data relevant to the manuscript are available from the authors upon request.

Received: 10 December 2020; Accepted: 1 June 2021;

Published online: 21 June 2021

References

- Qin, X. et al. Recent progress in stability of perovskite solar cells. *J. Semicond.* **38**, 11002 (2017).
- Yang, B. et al. Lead-free silver-bismuth halide double perovskite nanocrystals. *Angew. Chem. Int. Ed. Engl.* **57**, 5359–5363 (2018).
- Wu, C. et al. The dawn of lead-free perovskite solar cell: highly stable double perovskite Cs₂AgBiBr₆ film. *Adv. Sci.* **5**, 1700759 (2018).
- Hoye, R. L. Z. et al. Fundamental carrier lifetime exceeding 1 μs in Cs₂AgBiBr₆ double perovskite. *Adv. Mater. Interfaces* **5**, 1800464 (2018).
- Luo, J. et al. Cs₂AgInCl₆ double perovskite single crystals: parity forbidden transitions and their application for sensitive and fast UV photodetectors. *ACS Photonics* **5**, 398–405 (2018).
- Pan, W. et al. Cs₂AgBiBr₆ single-crystal X-ray detectors with a low detection limit. *Nat. Photonics* **11**, 726–732 (2017).
- Filip, M. R., Liu, X., Miglio, A., Hautier, G. & Giustino, F. Phase diagrams and stability of lead-free halide double perovskites Cs₂BB'X₆: B = Sb and Bi, B' = Cu, Ag, and Au, and X = Cl, Br, and I. *J. Phys. Chem. C* **122**, 158–170 (2018).
- Zhou, L., Xu, Y.-F., Chen, B.-X., Kuang, D.-B. & Su, C.-Y. Synthesis and photocatalytic application of stable lead-free Cs₂AgBiBr₆ perovskite nanocrystals. *Small* **14**, 1703762 (2018).
- Zhang, Z. et al. Stable and highly efficient photocatalysis with lead-free double-perovskite of Cs₂AgBiBr₆. *Angew. Chem. Int. Ed. Engl.* **58**, 7263–7267 (2019).
- Filip, M. R., Hillman, S., Haghghirad, A. A., Snaith, H. J. & Giustino, F. Band gaps of the lead-free halide double perovskites Cs₂BiAgCl₆ and Cs₂BiAgBr₆ from theory and experiment. *J. Phys. Chem. Lett.* **7**, 2579–2585 (2016).
- Zhou, J. et al. Composition design, optical gap and stability investigations of lead-free halide double perovskite Cs₂AgInCl₆. *J. Mater. Chem. A* **5**, 15031–15037 (2017).
- Luo, J. et al. Efficient and stable emission of warm-white light from lead-free halide double perovskites. *Nature* **563**, 541–545 (2018).
- Zhang, L. et al. Tuning emission and electron–phonon coupling in lead-free halide double perovskite Cs₂AgBiCl₆ under pressure. *ACS Energy Lett.* **4**, 2975–2982 (2019).
- Sapra, S., Mayilo, S., Klar, T. A., Rogach, A. L. & Feldmann, J. Bright white-light emission from semiconductor nanocrystals: by chance and by design. *Adv. Mater.* **19**, 569–572 (2007).
- Bowers, M. J., McBride, J. R. & Rosenthal, S. J. White-light emission from magic-sized cadmium selenide nanocrystals. *J. Am. Chem. Soc.* **127**, 15378–15379 (2005).
- Smith, M. D. & Karunadasa, H. I. White-light emission from layered halide perovskites. *Acc. Chem. Res.* **51**, 619–627 (2018).
- Wu, Z. et al. Broadband white-light emission with a high color rendering index in a two-dimensional organic–inorganic hybrid perovskite. *J. Mater. Chem. C* **6**, 1171–1175 (2018).
- Li, D. et al. White-light emission from a single organic compound with unique self-folded conformation and multistimuli responsiveness. *Chem. Sci.* **9**, 5709–5715 (2018).
- Yangu, A. et al. Optical investigation of broadband white-light emission in self-assembled organic–inorganic perovskite (C₆H₁₁NH₃)₂PbBr₄. *J. Phys. Chem. C* **119**, 23638–23647 (2015).
- Wang, S. et al. Highly efficient white-light emission in a polar two-dimensional hybrid perovskite. *Chem. Commun.* **54**, 4053–4056 (2018).
- Cortecchia, D. et al. Polaron self-localization in white-light emitting hybrid perovskites. *J. Mater. Chem. C* **5**, 2771–2780 (2017).
- Fugol', I. Y. Excitons in rare-gas crystals. *Adv. Phys.* **27**, 1–87 (1978).
- Luo, B. et al. Breaking forbidden transitions for emission of self-trapped excitons in two dimensional (F₂CHCH₂NH₃)₂CdBr₄ perovskite through Pb alloying. *J. Phys. Chem. Lett.* **11**, 199–205 (2020).
- Mao, L., Wu, Y., Stoumpos, C. C., Wasielewski, M. R. & Kanatzidis, M. G. White-light emission and structural distortion in new corrugated two-dimensional lead bromide perovskites. *J. Am. Chem. Soc.* **139**, 5210–5215 (2017).
- Liang, Y. et al. Broadband emission enhancement induced by self-trapped excited states in one-dimensional EAPbI₃ perovskite under pressure. *J. Phys. Chem. C* **124**, 8984–8991 (2020).
- Mao, L., Wu, Y., Stoumpos, C. C., Wasielewski, M. R. & Kanatzidis, M. G. White-light emission and structural distortion in new corrugated two-dimensional lead bromide perovskites. *J. Am. Chem. Soc.* **139**, 5210–5215 (2017).
- Dohner, E. R., Hoke, E. T. & Karunadasa, H. I. Self-assembly of broadband white-light emitters. *J. Am. Chem. Soc.* **136**, 1718–1721 (2014).
- Fang, Y. et al. Pressure-Induced Emission (PIE) and Phase Transition of a Two-dimensional Halide Double Perovskite (BA)₄AgBiBr₈ (BA=CH₃(CH₂)₃NH₃⁺). *Angew. Chem. Int. Ed.* **58**, 15249–15253 (2019).
- Zhang, L. et al. Tuning emission and electron–phonon coupling in lead-free halide double perovskite Cs₂AgBiCl₆ under pressure. *ACS Energy Lett.* **4**, 2975–2982 (2019).
- Ke, B. et al. Homo- and heterovalent doping-mediated self-trapped exciton emission and energy transfer in Mn-doped Cs₂Na_{1-x}AgBiCl₆ double perovskites. *J. Phys. Chem. Lett.* **11**, 340–348 (2020).
- Kshirsagar, A. S. & Nag, A. Synthesis and optical properties of colloidal Cs₂AgSb_{1-x}Bi_xCl₆ double perovskite nanocrystals. *J. Chem. Phys.* **151**, 161101 (2019).
- Yang, B. et al. Lead-free direct band gap double-perovskite nanocrystals with bright dual-color emission. *J. Am. Chem. Soc.* **140**, 17001–17006 (2018).
- Karmakar, A., Bernard, G. M., Meldrum, A., Oliynyk, A. O. & Michaelis, V. K. Tailorable indirect to direct band-gap double perovskites with bright white-light emission: decoding chemical structure using solid-state NMR. *J. Am. Chem. Soc.* **142**, 10780–10793 (2020).
- Cao, D. H., Stoumpos, C. C., Farha, O. K., Hupp, J. T. & Kanatzidis, M. G. 2D homologous perovskites as light-absorbing materials for solar cell applications. *J. Am. Chem. Soc.* **137**, 7843–7850 (2015).

35. Mao, L. et al. Chemical and structural diversity of hybrid layered double perovskite halides. *J. Am. Chem. Soc.* **141**, 19099–19109 (2019).
36. Volonakis, G. et al. Cs₂InAgCl₆: a new lead-free halide double perovskite with direct band gap. *J. Phys. Chem. Lett.* **8**, 772–778 (2017).
37. Slavney, A. H., Hu, T., Lindenberg, A. M. & Karunadasa, H. I. A bismuth-halide double perovskite with long carrier recombination lifetime for photovoltaic applications. *J. Am. Chem. Soc.* **138**, 2138–2141 (2016).
38. Alonso, J. A., Martínez-Lope, M. J., Casais, M. T. & Fernández-Díaz, M. T. Evolution of the Jahn–Teller distortion of MnO₆ octahedra in RMnO₃ perovskites (R = Pr, Nd, Dy, Tb, Ho, Er, Y): a neutron diffraction study. *Inorg. Chem.* **39**, 917–923 (2000).
39. Shannon, R. Revised effective ionic radii and systematic studies of interatomic distances in halides and chalcogenides. *Acta. Cryst.* **A32**, 751 (1976).
40. Manna, D. et al. Lattice dynamics and electron–phonon coupling in lead-free Cs₂AgIn_{1-x}Bi_xCl₆ Double Perovskite Nanocrystals. *J. Phys. Chem. Lett.* **11**, 2113–2120 (2020).
41. Gray, M. B., McClure, E. T. & Woodward, P. M. Cs₂AgBiBr_{6-x}Cl_x solid solutions-band gap engineering with halide double perovskites. *J. Mater. Chem. C* **7**, 9686–9689 (2019).
42. Mao, L. et al. Tunable white-light emission in single-cation-templated three-layered 2D perovskites (CH₃CH₂NH₃)₄Pb₃Br_{10-x}Cl_x. *J. Am. Chem. Soc.* **139**, 11956–11963 (2017).
43. Manna, D., Das, T. K. & Yella, A. Tunable and stable white light emission in Bi³⁺-Alloyed Cs₂AgInCl₆ double perovskite nanocrystals. *Chem. Mater.* **31**, 10063–10070 (2019).
44. Blaha, P. et al. WIEN2k: An APW+lo program for calculating the properties of solids. *J. Chem. Phys.* **152**, 74101 (2020).
45. Wang, X. et al. Atomistic mechanism of broadband emission in metal halide perovskites. *J. Phys. Chem. Lett.* **10**, 501–506 (2019).
46. Meng, W. et al. Parity-forbidden transitions and their impact on the optical absorption properties of lead-free metal halide perovskites and double perovskites. *J. Phys. Chem. Lett.* **8**, 2999–3007 (2017).
47. Tran, T. T., Panella, J. R., Chamorro, J. R., Morey, J. R. & McQueen, T. M. Designing indirect–direct bandgap transitions in double perovskites. *Mater. Horizons* **4**, 688–693 (2017).
48. Rakita, Y. et al. Tetragonal CH₃NH₃PbI₃ is ferroelectric. *Proc. Natl. Acad. Sci. USA* **114**, E5504–E5512 (2017).
49. Liao, W. Q. et al. A lead-halide perovskite molecular ferroelectric semiconductor. *Nat. Commun.* **6**, 1–7 (2015).
50. Guo, W. et al. Room-temperature ferroelectric material composed of a two-dimensional metal halide double perovskite for X-ray Detection. *Angew. Chem. Int. Ed. Engl.* **59**, 13879–13884 (2020).
51. Liu, Y., Jing, Y., Zhao, J., Liu, Q. & Xia, Z. Design optimization of lead-free perovskite Cs₂AgInCl₆:Bi nanocrystals with 11.4% photoluminescence quantum yield. *Chem. Mater.* **31**, 3333–3339 (2019).
52. Li, Q. et al. Pressure-induced remarkable enhancement of self-trapped exciton emission in one-dimensional CsCu₂I₃ with tetrahedral units. *J. Am. Chem. Soc.* **142**, 1786–1791 (2020).
53. Vietmeyer, F., Tchelidze, T., Tsou, V., Janko, B. & Kuno, M. Electric field-induced emission enhancement and modulation in individual cdse nanowires. *ACS Nano* **6**, 9133–9140 (2012).
54. Richards, G. A symmetry rule for predicting molecular structures. *J. Am. Chem. Soc.* **91**, 4947–4955 (1969).
55. Smit, W. M. A., Dirksen, G. J. & Stufkens, D. J. Infrared and Raman spectra of the elpasolites Cs₂NaSbCl₆ and Cs₂NaBiCl₆: evidence for a pseudo Jahn–Teller distorted ground state. *J. Phys. Chem. Solids* **51**, 189–196 (1990).
56. Płowaś, I., Bator, G., Jakubas, R. & Baran, J. Thermal, dielectric and vibrational properties of allylammonium chloroantimonates(III) and chlorobismuthates (III): [C 3H 5NH 3] 3[BiCl 6] and [C 3H 5NH 3] 3[SbCl 5]Cl. *Vib. Spectrosc.* **62**, 121–132 (2012).
57. Barrowcliffe, T., Beattie, I. R., Day, P. & Livingston, K. The vibrational spectra of some chloro-anions. *J. Chem. Soc.* <https://doi.org/10.1039/J19670001810> (1967).
58. Lines, M. E. & Glass, A. *Principles and Applications of Ferroelectrics and Related Materials*. (Oxford University Press, 2001).
59. Dietz, G. W. & Waser, R. How to analyse relaxation and leakage currents of dielectric thin films: Simulation of voltage-step and voltage-ramp techniques. *Integr. Ferroelectr.* **8**, 317–332 (1995).
60. Nagaraj, B., Aggarwal, S. & Ramesh, R. Influence of contact electrodes on leakage characteristics in ferroelectric thin films. *J. Appl. Phys.* **90**, 375–382 (2001).
61. Chen, H. M., Tsaur, S. W. & Lee, J. Y. M. Leakage current characteristics of lead-zirconate-titanate thin film capacitors for memory device applications. *Jpn. J. Appl. Phys.* **37**, 4056–4060 (1998).
62. Saladino, M. L. et al. Ce:YAG nanoparticles embedded in a PMMA matrix: preparation and characterization. *Langmuir* **26**, 13442–13449 (2010).
63. Perdew, J. P., Burke, K. & Ernzerhof, M. Generalized gradient approximation made simple. *Phys. Rev. Lett.* **77**, 3865–3868 (1996).
64. Tran, F. & Blaha, P. Accurate band gaps of semiconductors and insulators with a semilocal exchange–correlation potential. *Phys. Rev. Lett.* **102**, 5–8 (2009).

Acknowledgements

This project is funded by (i) Science & Engineering Research Board (SERB), Department of Science & Technology, Government of India under Extra Mural Research Funding (sanction number EMR/2017/000181) and (ii) Nanomission, Department of Science & Technology, Government of India (sanction number DST/NM/NT/2018/82). Tamilselvan Appadurai acknowledges funding from DST-National Postdoctoral Fellowship (sanction number PDF/2017/001952) and IIT-Madras Institute Postdoctoral Fellowship. AKC acknowledges the funding from MHRD under Institute of Eminence grant from IIT-Madras (sanction number 11/9/2019-U.3(A)). We thank Dr. Babu Varghese, SAIF, IIT-Madras, for assisting us in solving the single-crystal structures.

Author contributions

The manuscript was written through the contributions of all authors. TA, PS, and AKC planned all the experiments. PS synthesized single-crystals of halide perovskite and carried out single-crystal emission studies. Single-crystal XRD experiments were carried out by SA. Crystal structures are solved by TA and SA. All the other experiments, including PXRD, Rietveld refinement, absorption, PL, lifetime decay, bias-dependent studies, excitation spectra, Raman studies, P–E loop measurements, staircase and pulse voltage measurements, were carried out by TA. RK and BRKN planned the DFT simulations work in consultation with TA and AKC. RK executed all the DFT calculations. BRKN supervised the DFT simulations work. AKC coordinated the experiments and simulation work and supervised the entire project. All authors have given approval to the final version of the manuscript.

Competing interests

The authors declare no competing interests

Additional information


Supplementary information The online version contains supplementary material available at <https://doi.org/10.1038/s43246-021-00172-9>.

Correspondence and requests for materials should be addressed to B.R.K.N. or A.K.C.

Peer review information *Communications Materials* thanks the anonymous reviewers for their contribution to the peer review of this work. Primary Handling Editors: Andreja Benčan Golob, Aldo Isidori.

Reprints and permission information is available at <http://www.nature.com/reprints>

Publisher's note Springer Nature remains neutral with regard to jurisdictional claims in published maps and institutional affiliations.

 **Open Access** This article is licensed under a Creative Commons Attribution 4.0 International License, which permits use, sharing, adaptation, distribution and reproduction in any medium or format, as long as you give appropriate credit to the original author(s) and the source, provide a link to the Creative Commons license, and indicate if changes were made. The images or other third party material in this article are included in the article's Creative Commons license, unless indicated otherwise in a credit line to the material. If material is not included in the article's Creative Commons license and your intended use is not permitted by statutory regulation or exceeds the permitted use, you will need to obtain permission directly from the copyright holder. To view a copy of this license, visit <http://creativecommons.org/licenses/by/4.0/>.

© The Author(s) 2021